axioms

Article

A Comprehensive Model and Numerical Study of Shear Flow in Compressible Viscous Micropolar Real Gases

Nelida Črnjarić † **and Ivan Dražić** *,†

Faculty of Engineering, University of Rijeka, Vukovarska 58, 51000 Rijeka, Croatia; nelida.crnjaric@riteh.uniri.hr
* Correspondence: ivan.drazic@riteh.uniri.hr; Tel.: +385-51-651-482
† These authors contributed equally to this work.

Abstract: Understanding shear flow behavior in compressible, viscous, micropolar real gases is essential for both theoretical advancements and practical engineering applications. This study develops a comprehensive model that integrates micropolar fluid theory with compressible flow dynamics to accurately describe the behavior of real gases under shear stress. We formulate the governing equations by incorporating viscosity and micropolar effects and transform the obtained system into the mass Lagrangian coordinates. Two numerical methods, Faedo–Galerkin approximation and finite-difference methods, are used to solve it. These methods are compared using several benchmark examples to assess their accuracy and computational efficiency. Both methods demonstrate good performance, achieving equally precise results in capturing essential flow characteristics. However, the finite-difference method offers advantages in speed, stability, and lower computational demands. This research bridges gaps in existing models and establishes a foundation for further investigations into complex flow phenomena in micropolar real gases.

Keywords: shear flow; compressible flow; real gas; micropolar fluids; Faedo–Galerkin method; finite-difference method

MSC: 35Q35; 76M25; 76N99

check for updates

Citation: Črnjarić, N.; Dražić, I. A Comprehensive Model and Numerical Study of Shear Flow in Compressible Viscous Micropolar Real Gases. *Axioms* **2024**, *13*, 845. https://doi.org/10.3390/axioms13120845

Academic Editor: Satyvir Singh

Received: 28 October 2024
Revised: 25 November 2024
Accepted: 29 November 2024
Published: 2 December 2024

Copyright: © 2024 by the authors. Licensee MDPI, Basel, Switzerland. This article is an open access article distributed under the terms and conditions of the Creative Commons Attribution (CC BY) license (https://creativecommons.org/licenses/by/4.0/).

1. Introduction

Understanding shear flows in compressible, viscous micropolar real gases is crucial for advancing theoretical and engineering applications. Traditional fluid models often overlook microstructural effects like microrotations and couple stresses. This study integrates micropolar fluid theory with real gas dynamics, offering a more accurate representation of such flows. Additionally, numerical methods like Faedo–Galerkin and finite differences are used to analyze shear flow characteristics, bridging gaps in current research and paving the way for future studies.

1.1. Micropolar Continuum and Compressible Micropolar Fluids

The micropolar continuum extends classical mechanics by incorporating translational and rotational degrees of freedom, allowing for the modeling of materials with significant microstructural features. Initially introduced by the Cosserat brothers [1] and later refined by A.C. Eringen [2], this theory captures microrotations and internal moments, making it particularly useful for describing granular media, composites, and biomaterials.

Micropolar fluid theory further generalizes classical fluid models by accounting for internal cell rotations and micromoments, enabling a deeper understanding of flows in colloidal suspensions, emulsions, and biological fluids [3]. Compressible micropolar fluids extend this framework by incorporating fluid compressibility, allowing for the detailed modeling of compressible systems like gases with significant microstructural effects [2]. The governing equations build on the Navier–Stokes framework, integrating terms for microrotational dynamics and internal moments [4].

This advanced theory is essential for high-velocity and high-pressure flows, where conventional models fail to account for compressibility and microstructural interactions. Micropolar effects are particularly critical in micro- and nanodomains, where internal rotations and moments significantly influence fluid behavior, making this approach invaluable for applications in micro- and nanotechnology [5].

1.2. Micropolar Real Gas

The ideal gas model, while useful under low pressures and high temperatures, fails to account for intermolecular forces and molecular size, which become significant at high pressures [6]. Real gas models, with nonlinear pressure–volume–temperature relationships, offer a more accurate depiction of compressibility and thermodynamic behavior [7].

In compressible micropolar fluid theory, incorporating real gas behavior is crucial for capturing the interplay between compressibility and microrotational dynamics [2]. This integration enhances model accuracy, particularly in highly compressible systems where small volumetric changes strongly influence microrotations. Such a robust approach is vital for precise predictions in applications like aerospace engineering and industrial gas processes [8,9].

1.3. Compressible Shear Flow

Shear flow involves fluid layers moving at different velocities, generating shear stress due to velocity gradients, as seen in viscous flow between moving and stationary plates. In classical simple shear flow, the fluid exhibits laminar motion without internal rotation, with shear stress proportional to the velocity gradient under Newtonian, incompressible assumptions.

In compressible micropolar real gases, the flow becomes more complex. Compressibility and microrotational effects introduce normal velocity components and modify shear stress through couple stresses and real gas dynamics. While dominant changes occur parallel to the plates, small but significant variations in other directions must be considered to accurately capture fluid behavior.

The governing equations include continuity, momentum, angular momentum for microrotations, and energy conservation, ensuring a comprehensive description of compressible shear flow dynamics.

1.4. Literature Review and Important Results

Shear flow in compressible fluids has been explored in foundational works [10–12], with further studies addressing initial-boundary value problems and their solution properties [13,14]. For classical, non-micropolar real fluids, research has focused on solution existence, regularity, and stabilization, particularly in one-dimensional settings [15–20], with applications to thermal explosion phenomena [21–23].

Micropolar fluid dynamics, encompassing incompressible and compressible theories, has been widely studied for its mathematical properties and diverse applications in fields such as chemistry, physics, metallurgy, biomedicine, and engineering [24–29]. Compressible micropolar fluid models were first introduced by N. Mujaković [30] and extended to three-dimensional cases with spherical or cylindrical symmetry, establishing the existence and uniqueness of solutions [31].

In one-dimensional micropolar real fluids, studies have demonstrated local and global existence and uniqueness of solutions, with recent investigations into thermal explosion phenomena [32]. Numerical methods for micropolar fluids include the Faedo–Galerkin method [32] and finite-difference methods [33,34], both of which provide approximate solutions and establish method convergence for proving solution existence.

1.5. Research Aims and Objectives

This research investigates the shear flow of a compressible, viscous, real micropolar fluid, advancing previous studies by incorporating a realistic equation of state to capture non-ideal fluid characteristics. The study formulates the governing initial-boundary value

problem and develops numerical solutions using the Faedo–Galerkin and finite-difference methods, focusing on stability, convergence, and computational efficiency to provide a robust framework for modeling real micropolar fluids.

1.6. Structure of the Article

This paper outlines the derivation of the model for compressible micropolar real gases (Section 2), the numerical methods used (Sections 3 and 4), and their comparative performance through numerical experiments (Section 5), concluding with key findings and future research directions (Section 6).

2. Derivation of the Model

In this section, we derive the governing equations and boundary conditions for a compressible, micropolar fluid model, specifically in the context of shear flow and real gas behavior. This derivation combines classical conservation laws with adjustments to capture the unique interactions arising from compressibility, microrotation, and real gas dynamics within the shear flow framework.

2.1. Conservation Laws

To accurately model the behavior of compressible micropolar fluids, particularly in shear flow scenarios involving real gases, it is essential to ground the formulation in fundamental physical principles. This model is grounded in the local forms of conservation laws governing mass, linear momentum, angular momentum, and energy. These laws offer a thorough description of how the fluid evolves over time and through space by accounting for the conservation of key physical quantities.

The conservation of angular momentum is crucial for micropolar fluids, where each fluid element can rotate independently of its neighbors, ensuring that internal microrotations and couple stresses are accurately incorporated into the model. Energy conservation links the thermodynamic properties of the gas with the mechanical and microrotational motion of the fluid. For real gases, the complex relationship between pressure, density, and temperature requires including the energy equation to accurately capture gas behavior under varying thermal and mechanical conditions.

The aforementioned conservation laws, as outlined in [3], are expressed in the following forms, in the same order as previously described:

$$\dot{\rho} = -\rho \nabla \cdot \mathbf{v}, \tag{1}$$

$$\rho \dot{\mathbf{v}} = \nabla \cdot \mathbf{T} + \rho \mathbf{f}, \tag{2}$$

$$\rho j_I \dot{\boldsymbol{\omega}} = \nabla \cdot \mathbf{C} + \mathbf{T}_x + \rho \mathbf{g}, \tag{3}$$

$$\rho \dot{E} = -\nabla \cdot \mathbf{q} + \mathbf{T} : \nabla \mathbf{v} + \mathbf{C} : \nabla \boldsymbol{\omega} - \mathbf{T}_x \cdot \boldsymbol{\omega}, \tag{4}$$

where ρ is the mass density, $\mathbf{v}$ the velocity, $\boldsymbol{\omega}$ the microrotation velocity, and E the internal energy density. The positive constant j_i represents the microinertia density, which characterizes the distribution of rotational inertia in the micropolar fluid. The tensor $\mathbf{T}$ represents the stress tensor, $\mathbf{C}$ is the couple stress tensor, $\mathbf{q}$ is the heat flux density vector, $\mathbf{f}$ is the body force density, and $\mathbf{g}$ denotes the body couple density. For simplicity reasons, we will also assume that

$$\mathbf{f} = \mathbf{g} = 0. \tag{5}$$

The vector $\mathbf{T}_x$ in Equations (3) and (4) is an axial vector with Cartesian components $(\mathbf{T}_x)i = \varepsilon_{ijk}\mathbf{T}_{jk}$, where ε_{ijk} is the Levi-Civita symbol and δ_{ij} is the Kronecker delta. The Levi-Civita symbol ε_{mij} reappears in subsequent equations, and we assume Einstein summation notation throughout. The colon operator in Equation (4) represents the scalar product of tensors, for example, $\mathbf{T} : \nabla \mathbf{v} = \mathbf{T}_{ji}\mathbf{v}_{i,j}$. The dot operator in Equations (1)–(4) represents the material derivative:

$$\dot{\mathbf{b}} = \partial_t \mathbf{b} + (\nabla \mathbf{b}) \cdot \mathbf{v}. \tag{6}$$

To complete the system of governing equations, we introduce constitutive equations for the stress tensor **T** and couple stress tensor **C**. These describe the relationship between stresses, microrotations, and deformation rates, which are essential for accurately capturing micropolar fluid behavior. In the context of micropolar real gases, the constitutive relations for **T** and **C** account for both the traditional viscous effects and the additional rotational degrees of freedom that are inherent to these fluids.

The stress tensor **T** is given by the following expression:

$$\mathbf{T}_{ij} = (-P + \lambda \mathbf{v}_{k,k})\delta_{ij} + \mu(\mathbf{v}_{i,j} + \mathbf{v}_{j,i}) + \mu_r(\mathbf{v}_{j,i} - \mathbf{v}_{i,j}) - 2\mu_r \varepsilon_{mij}\boldsymbol{\omega}_m, \tag{7}$$

where P denotes the pressure, λ and μ are the viscosity coefficients, and μ_r is the coefficient of microrotational viscosity. Here, $\boldsymbol{\omega}_m$ are the components of the microrotation velocity. This formulation captures the symmetric and antisymmetric parts of the velocity gradient tensor and the effects of microrotations, essential for representing microstructural dynamics in micropolar fluids.

The couple stress tensor **C** is expressed as:

$$\mathbf{C}_{ij} = c_0 \boldsymbol{\omega}_{k,k}\delta_{ij} + c_d(\boldsymbol{\omega}_{i,j} + \boldsymbol{\omega}_{j,i}) + c_a(\boldsymbol{\omega}_{j,i} - \boldsymbol{\omega}_{i,j}), \tag{8}$$

where c_0, c_d, and c_a are microviscosity coefficients. This tensor similarly reflects the symmetric and antisymmetric contributions of the microrotation field's derivatives.

To ensure physical consistency, the viscosity and microviscosity coefficients must satisfy the Clausius–Duhem inequalities, which guarantee positive dissipation in the system. The inequalities are:

$$\mu \geq 0, \qquad 3\lambda + 2\mu \geq 0, \qquad \mu_r \geq 0, \tag{9}$$

for viscosity coefficients and

$$c_d \geq 0, \quad 3c_0 + 2c_d \geq 0, \quad |c_d - c_a| \leq c_d + c_a, \tag{10}$$

for microviscosity coefficients. These conditions ensure thermodynamically admissible material behavior, avoiding non-physical outcomes like negative energy dissipation.

2.2. Real Gas

To model real gas behavior, we introduce an appropriate equation of state as in [35]:

$$P(\rho, \theta) = f(\rho) + \theta g(\rho), \tag{11}$$

where P is the pressure, ρ is the mass density, θ is the absolute temperature, and $f(\rho)$ and $g(\rho)$ are specified functions of the density. This form implies that, at a fixed density, pressure depends linearly on temperature.

This linear dependence is a useful approximation for real gases, as, at moderate pressures and temperatures, the pressure-temperature relationship is approximately linear at constant density. This observation holds for many gases across various thermodynamic states, making the model mathematically tractable and physically realistic [36].

We assume pressure consists of two components: external, $f(\rho)$, representing atmospheric or environmental influences, and internal, $g(\rho)$, related to the fluid's intrinsic behavior. In high-pressure systems, external effects are typically negligible compared to internal fluid dynamics. Since real fluids are characterized by dominant internal forces, we neglect external pressure in our model to focus on internal dynamics.

Internal pressure, $g(\rho)$, captures the fluid's intrinsic behavior and follows a power-law relationship with density:

$$g(\rho) = R\rho^p, \tag{12}$$

where $p \geq 1$ is the pressure exponent and R a positive constant. This model accounts for nonlinear effects like intermolecular forces and molecular volume corrections, especially significant at higher densities. These non-ideal behaviors are essential for accurately modeling real fluids, particularly when the ideal gas law is insufficient (see [15,20,37]). Considering these factors, we adopt the following equation of state:

$$P(\rho, \theta) = R\rho^p\theta, \tag{13}$$

using the previously introduced notation.

The equation of state for a real gas affects the relationship between internal energy and temperature by accounting for non-ideal gas behavior, such as intermolecular forces and molecular volume. The differential form of internal energy for a real gas is (see [38]):

$$dE = c_v d\theta + [\theta\partial_\theta P - P]dV, \tag{14}$$

where c_v is the specific heat at constant volume, and V is the volume. Substituting the equation of state (13) yields:

$$E = c_v\theta, \tag{15}$$

indicating that internal energy depends only on temperature despite the non-linearities of the equation of state. This assumption simplifies the energy equation and is valid in many cases where temperature is the dominant factor, even for real gases.

To model heat conduction, we apply Fourier's law, describing heat flow due to temperature gradients:

$$\mathbf{q} = -k_\theta\nabla\theta, \tag{16}$$

where $\mathbf{q}$ is the heat flux and $k_\theta \geq 0$ is the heat conduction coefficient. Fourier's law governs the rate of heat conduction, influencing temperature distributions over time while keeping internal energy dependent solely on temperature and leaving the equation of state unchanged.

2.3. Governing Equations

Substituting Equations (7), (8), (13), (15) and (16) into the governing system (1)–(4), along with the material derivative (6) and simplification (5), yields the following system:

$$\partial_t\rho = -(\nabla\rho)\cdot\mathbf{v} - \rho\nabla\cdot\mathbf{v}, \tag{17}$$

$$\rho\,\partial_t\mathbf{v} = -\rho((\nabla\mathbf{v})\cdot\mathbf{v}) - R\nabla(\rho^p\theta) + (\lambda+\mu-\mu_r)\nabla(\nabla\cdot\mathbf{v}) + (\mu+\mu_r)\Delta\mathbf{v} + 2\mu_r\nabla\times\boldsymbol{\omega}, \tag{18}$$

$$\begin{aligned} j_I\rho\,\partial_t\boldsymbol{\omega} = &-j_I\rho((\nabla\boldsymbol{\omega})\cdot\mathbf{v}) + 2\mu_r(\nabla\times\mathbf{v} - 2\boldsymbol{\omega}) \\ &+(c_0+c_d-c_a)\nabla(\nabla\cdot\boldsymbol{\omega}) + (c_d+c_a)\Delta\boldsymbol{\omega}, \end{aligned} \tag{19}$$

$$\begin{aligned} c_v\rho\,\partial_t\theta = &-c_v\rho(\nabla\theta)\cdot\mathbf{v} + k_\theta\Delta\theta - R\rho^p\theta(\nabla\cdot\mathbf{v}) + \lambda(\nabla\cdot\mathbf{v})^2 \\ &+\frac{\mu}{2}(\nabla\mathbf{v}+(\nabla\mathbf{v})^T) : (\nabla\mathbf{v}+(\nabla\mathbf{v})^T) + 4\mu_r\left(\frac{1}{2}\nabla\times\mathbf{v} - \boldsymbol{\omega}\right)^2 \\ &+c_0(\nabla\cdot\boldsymbol{\omega})^2 + (c_d+c_a)\nabla\boldsymbol{\omega} : \nabla\boldsymbol{\omega} + (c_d-c_a)\nabla\boldsymbol{\omega} : (\nabla\boldsymbol{\omega})^T. \end{aligned} \tag{20}$$

This system is defined on the domain $Q_T = \Omega\times(0,T)$, where $T > 0$ is arbitrary and $\Omega \subset \mathbf{R}^3$.

2.4. Initial and Boundary Conditions

To describe flows governed by Equations (17)–(20), we introduce the following initial conditions:

$$\rho(\mathbf{x},0) = \rho_0(\mathbf{x}), \quad \mathbf{v}(\mathbf{x},0) = \mathbf{v}_0(\mathbf{x}), \quad \boldsymbol{\omega}(\mathbf{x},0) = \boldsymbol{\omega}_0(\mathbf{x}), \quad \theta(\mathbf{x},0) = \theta_0(\mathbf{x}), \tag{21}$$

for all $\mathbf{x} \in \Omega$, where Ω is the spatial domain.

Boundary conditions are specified to capture behavior at the spatial domain boundaries. For the velocity field, we impose a Dirichlet boundary condition prescribing velocity on the boundary $\partial\Omega$ over time:

$$\mathbf{v}|_{\partial\Omega} = \mathbf{v}_1(t), \tag{22}$$

for $0 < t < T$, where $\mathbf{v}_1(t)$ is a known boundary velocity function.

For the microrotation field, a homogeneous boundary condition is commonly applied in studies of compressible micropolar fluids. Accordingly, we set:

$$\boldsymbol{\omega}|_{\partial\Omega} = \mathbf{0}, \tag{23}$$

meaning there is no microrotation at the boundary.

For the temperature field, we apply a Neumann boundary condition, assuming the domain acts as a thermally insulated wall with no heat flux across the boundary:

$$\left.\frac{\partial\theta}{\partial\mathbf{n}}\right|_{\partial\Omega} = 0, \tag{24}$$

where $\mathbf{n}$ is the outward normal vector. This condition enforces thermal insulation by preventing heat exchange through the boundary.

2.5. Shear Flow

Shear flow involves the movement of fluid layers parallel to each other, with each layer flowing at a different velocity, creating a velocity gradient. This flow is typically modeled between two parallel plates: one stationary, the other moving, generating shear between fluid layers. This setup establishes symmetry in the system, influencing the spatial variables governing fluid behavior.

We use a Cartesian coordinate system with axes x, y and z, where gravitational force acts in the negative x-direction. The lower plate is at $x = 0$ and remains fixed, while the upper plate, positioned at $x = h$ (where $h > 0$), moves irrotationally in the plane $x = h$, inducing no internal rotation in the fluid layers. Thermally, both plates are assumed insulated, preventing heat transfer through the boundaries.

In shear flow, fluid moves in layers, with each layer's velocity depending only on its distance from the plates. Since the flow is confined between two infinite parallel plates, translational symmetry exists in the y and z directions. Consequently, all physical quantities vary only with the vertical coordinate x, reducing the problem to a one-dimensional case:

$$\rho(\mathbf{x}, t) = \rho(x, t), \quad \theta(\mathbf{x}, t) = \theta(x, t), \tag{25}$$

$$\mathbf{v}(\mathbf{x}, t) = \mathbf{v}(x, t) = (u(x, t), v_2(x, t), v_3(x, t)), \tag{26}$$

$$\boldsymbol{\omega}(\mathbf{x}, t) = \boldsymbol{\omega}(x, t) = (w(x, t), \omega_2(x, t), \omega_3(x, t)), \tag{27}$$

for $(x, t) \in (0, h) \times (0, T)$.

Please note that while the fluid flow remains three-dimensional, the problem reduces to a one-dimensional case. In this context, the initial conditions in (21) are:

$$\rho(x, 0) = \rho_0(x), \quad \theta(x, 0) = \theta_0(x), \tag{28}$$

$$\mathbf{v}(x, 0) = (u_0(x), v_{20}(x), v_{30}(x)), \tag{29}$$

$$\boldsymbol{\omega}(x, 0) = (w_0(x), \omega_{20}(x), \omega_{30}(x)), \tag{30}$$

for $x \in [0, h]$. The boundary conditions (22)–(24) take the form:

$$\mathbf{v}(0, t) = \mathbf{0}, \quad \mathbf{v}(h, t) = \mathbf{a}(t), \tag{31}$$

$$\boldsymbol{\omega}(0, t) = \boldsymbol{\omega}(h, t) = \mathbf{0}, \tag{32}$$

$$\partial_x \theta(0,t) = \partial_x \theta(h,t) = 0, \tag{33}$$

for $t \in [0,T]$, where $\mathbf{a}(t) = (0, a_1(t), a_2(t))$ defines the upper plate's motion.

2.6. Reduced System of Governing Equations

Reducing the system (17)–(20) from three dimensions to one through symmetry considerations yields the Eulerian form of the governing equations. Since this reduction is addressed in earlier works (see [39]), and the transition to Lagrangian form is analogous, we directly present the system in Lagrangian notation to highlight specific differences introduced by the modified equation of state.

The Lagrangian framework allows for tracking individual fluid particles as they traverse the flow, which is especially useful in compressible and micropolar fluid systems. It provides a clearer representation of changes in material derivatives for each particle, essential for capturing complex dynamics of real gases under modified pressure conditions. Presenting the model in Lagrangian form enables a more intuitive and precise analysis, avoiding repetition of the standard Eulerian-to-Lagrangian transition.

In this work, we adopt mass coordinates within the Lagrangian framework to effectively capture the dynamics of a real fluid, particularly for compressible and non-ideal fluids where mass conservation and nonlinear effects are essential. Mass-based coordinates allow for individual tracking of each fluid particle's mass, simplifying the treatment of compressibility and deformation. This approach inherently satisfies mass conservation, especially in real gases and compressible flows where significant density changes can occur. Additionally, it streamlines the mathematical description of fluid property evolution, particularly in the context of nonlinear compressibility effects governed by a modified equation of state.

The transition to mass-based Lagrangian coordinates involves expressing governing equations in terms of mass rather than spatial position. In the one-dimensional case, the mass coordinate $\eta(\xi)$ relates to the spatial coordinate ξ via the cumulative mass function:

$$\eta(\xi) = \int_0^{\xi} \rho_0(s) ds, \tag{34}$$

where $\rho_0(s)$ is the initial density distribution, and ξ is the particle's initial reference position, or Lagrangian coordinate.

If $\rho_0(s) > 0$ for all $s \in (0,h)$, the function η is invertible, allowing us to define a normalized mass coordinate:

$$q = \frac{\eta(\xi)}{L}, \tag{35}$$

where

$$L = \int_0^h \rho_0(s), ds \tag{36}$$

is the total mass of the fluid in the domain $[0,h]$. The assumption of a positive initial density throughout the domain is physically justified, as it ensures the domain is fully occupied by the fluid, with no vacuum states. Thus, we assume the initial mass density is bounded below by a positive constant:

$$\rho_0(s) \geq m, \tag{37}$$

for all $s \in]0,h[$, where m is a positive real number. This lower bound ensures that the cumulative mass function $\eta(\xi)$ is strictly increasing and invertible, allowing us to define the normalized mass coordinate.

In this new coordinate system (q,t), the spatial domain transforms to $(0,1)$. Thus, the domain for our problem becomes:

$$Q_T = (0,1) \times (0,T). \tag{38}$$

The relationship between Eulerian and mass-based Lagrangian coordinates is given by:

$$\xi(q,t) = \xi_0(q) + \int_0^t u(\tau)d\tau, \quad \xi_0(q) = \eta^{-1}(Lq). \tag{39}$$

We now present the initial-boundary value problem in mass Lagrangian coordinates. However, in numerical experiments, results will be displayed in Eulerian coordinates, which are more suitable for interpretation, even though the problem is formulated in the Lagrangian framework. For simplicity, we replace the variable q with x throughout, as this substitution does not introduce ambiguity.

The detailed derivation of the governing equations is omitted here, as it closely follows the steps in [32]. Readers may refer to that work for the full derivation. While the derivation is similar, this study extends the model and applies it to a more complex physical system. The corresponding initial-boundary value problem is presented below.

$$\partial_t \rho + L^{-1}\rho^2 \partial_x u = 0, \tag{40}$$

$$\partial_t u = -L^{-1}R\partial_x(\rho^p\theta) + L^{-2}(\lambda+2\mu)\partial_x(\rho\,\partial_x u), \tag{41}$$

$$\partial_t \mathbf{u} = L^{-2}(\mu+\mu_r)\partial_x(\rho\,\partial_x \mathbf{u}) + 2L^{-1}\mu_r \nabla\times\mathbf{w}, \tag{42}$$

$$j_I \partial_t w = L^{-2}(c_0+2c_d)\partial_x(\rho\,\partial_x w) - 4\mu_r\frac{w}{\rho}, \tag{43}$$

$$j_I \partial_t \mathbf{w} = L^{-2}(c_d+c_a)\partial_x(\rho\,\partial_x \mathbf{w}) - \frac{4\mu_r}{\rho}\mathbf{w} + 2L^{-1}\mu_r\nabla\times\mathbf{u}, \tag{44}$$

$$\begin{aligned} c_v\partial_t\theta = {} & L^{-2}k_\theta\partial_x(\rho\partial_x\theta) - L^{-1}R\rho^p\theta\partial_x u + L^{-2}(\lambda+2\mu)\rho(\partial_x u)^2 + L^{-2}(\mu+\mu_r)\rho|\partial_x\mathbf{u}|^2 \\ & + 4\mu_r\frac{w^2}{\rho} + 4\mu_r\frac{|\mathbf{w}|^2}{\rho} - 4L^{-1}\mu_r(\nabla\times\mathbf{u})\cdot\mathbf{w} + L^{-2}(c_0+2c_d)\rho(\partial_x w)^2 + \\ & L^{-2}(c_d+c_a)\rho|\partial_x\mathbf{w}|^2, \end{aligned} \tag{45}$$

for $(x,t)\in(0,1)\times(0,T)$,

$$\rho(x,0) = \rho_0(x), \quad \theta(x,0) = \theta_0(x), \tag{46}$$

$$u(x,0) = u_0(x), \quad \mathbf{u}(x,0) = (0, v_{20}, v_{30})(x), \tag{47}$$

$$w(x,0) = w_0(x), \quad \mathbf{w}(x,0) = (0, \omega_{20}, \omega_{30})(x), \tag{48}$$

for $x\in[0,1]$,

$$u(0,t) = u(1,t) = 0, \tag{49}$$

$$\mathbf{u}(0,t) = \mathbf{0}, \quad \mathbf{u}(1,t) = \mathbf{a}(t) = (0, a_1(t), a_2(t)), \tag{50}$$

$$w(0,t) = w(1,t) = 0, \quad \mathbf{w}(0,t) = \mathbf{w}(1,t) = \mathbf{0}, \tag{51}$$

$$\partial_x\theta(0,t) = \partial_x\theta(1,t) = 0, \tag{52}$$

for $t\in[0,T]$, where we introduced the vectors

$$\mathbf{u} = (0, v_2, v_3), \quad \mathbf{w} = (0, \omega_2, \omega_3). \tag{53}$$

3. Faedo–Galerkin Approximations

The Faedo–Galerkin method is a robust numerical approach for approximating solutions to partial differential equations by expanding unknown functions over a finite set of basis functions from an appropriate function space. Applying this method reduces problem (40)–(52) to a system of ordinary differential equations solvable numerically, aiming to produce accurate approximations of the original problem's solution.

To successfully apply the Faedo–Galerkin method, we homogenize the boundary conditions, simplifying boundary term handling and ensuring compatibility with chosen

basis functions. This homogenization is essential for accurately capturing system behavior at the boundaries. To homogenize the boundary condition for $\mathbf{u}(1,t)$, we introduce the substitution:

$$\mathbf{V}(x,t) = \mathbf{u}(x,t) - \mathbf{h}(x,t), \tag{54}$$

where

$$\mathbf{h}(x,t) = \frac{\mathbf{a}(t)}{A} \int_0^x \frac{dy}{\rho(y,t)}, \tag{55}$$

and

$$A = \int_0^1 \frac{dx}{\rho_0(x)}. \tag{56}$$

To show that the new variable $\mathbf{V}(x,t)$ satisfies homogeneous boundary conditions, we use the identity:

$$\int_0^1 \frac{dx}{\rho(x,t)} = \int_0^1 \frac{dx}{\rho_0(x)} = A, \tag{57}$$

which follows from rewriting Equation (38) as

$$\partial_t \left(\frac{1}{\rho}\right) = L^{-1}\partial_x u. \tag{58}$$

Integrating (58) over x and t, and applying boundary conditions for $\mathbf{u}$, yields (57). Using this identity together with boundary condition (50), we find:

$$\mathbf{V}(1,t) = \mathbf{u}(1,t) - \mathbf{h}(1,t) = \mathbf{a}(t) - \frac{\mathbf{a}(t)}{A} \int_0^1 \frac{dy}{\rho(y,t)} = 0. \tag{59}$$

The system in terms of the new variables is:

$$\partial_t \rho + L^{-1}\rho^2 \partial_x u = 0, \tag{60}$$

$$\partial_t u = -L^{-1}R\partial_x(\rho^p\theta) + L^{-2}(\lambda+2\mu)\partial_x(\rho\,\partial_x u), \tag{61}$$

$$\partial_t \mathbf{V} = L^{-2}(\mu+\mu_r)\partial_x(\rho\,\partial_x \mathbf{V}) + 2L^{-1}\mu_r \nabla\times\mathbf{w} - \partial_t \mathbf{h}, \tag{62}$$

$$j_I \partial_t w = L^{-2}(c_0+2c_d)\partial_x(\rho\,\partial_x w) - 4\mu_r \frac{w}{\rho}, \tag{63}$$

$$j_I \partial_t \mathbf{w} = L^{-2}(c_d+c_a)\partial_x(\rho\,\partial_x \mathbf{w}) - \frac{4\mu_r}{\rho}\mathbf{w} + 2L^{-1}\mu_r \nabla\times\mathbf{V} + 2L^{-1}\mu_r\nabla\times\mathbf{h}, \tag{64}$$

$$\begin{aligned} c_v\partial_t\theta = {} & L^{-2}k_\theta\partial_x(\rho\,\partial_x\theta) - L^{-1}R\rho^p\theta\partial_x u + L^{-2}(\lambda+2\mu)\rho(\partial_x u)^2 + \\ & L^{-2}(\mu+\mu_r)\rho|\partial_x\mathbf{V}|^2 + 2L^{-2}(\mu+\mu_r)\rho\partial_x\mathbf{V}\partial_x\mathbf{h} + L^{-2}(\mu+\mu_r)\rho|\partial_x\mathbf{h}|^2 + 4\mu_r\frac{w^2}{\rho} + \\ & 4\mu_r\frac{|\mathbf{w}|^2}{\rho} - 4L^{-1}\mu_r(\nabla\times\mathbf{V})\cdot\mathbf{w} - 4L^{-1}\mu_r(\nabla\times\mathbf{h})\cdot\mathbf{w} + L^{-2}(c_0+2c_d)\rho(\partial_x w)^2 \\ & + L^{-2}(c_d+c_a)\rho|\partial_x\mathbf{w}|^2, \end{aligned} \tag{65}$$

for $(x,t) \in (0,1)\times(0,T)$, with homogeneous boundary conditions

$$u(0,t) = u(1,t) = 0, \quad \mathbf{V}(0,t) = \mathbf{V}(1,t) = \mathbf{0}, \tag{66}$$

$$w(0,t) = w(1,t) = 0, \quad \mathbf{w}(0,t) = \mathbf{w}(1,t) = \mathbf{0}, \tag{67}$$

$$\partial_x\theta(0,t) = \partial_x\theta(1,t) = 0, \tag{68}$$

for $t \in [0,T]$, and initial conditions

$$\rho(x,0) = \rho_0(x), \quad u(x,0) = u_0(x), \tag{69}$$

$$\mathbf{V}(x,0) = \mathbf{V}_0(x) = \mathbf{u}_0(x) - \frac{\mathbf{a}(0)}{A}\int_0^x \frac{dy}{\rho_0(y)}, \tag{70}$$

$$w(x,0) = w_0(x), \quad \mathbf{w}(x,0) = \mathbf{w}_0(x), \tag{71}$$

$$\theta(x,0) = \theta_0(x), \tag{72}$$

for $x \in [0,1]$.

We will obtain a numerical solution to the problem (65)–(72) using the Faedo–Galerkin method, following the approach outlined in [32,39] and the framework in [40]. Specifically, for a chosen $n \in \mathbf{N}$ we define approximate solutions

$$\rho^n, u^n, \mathbf{V}^n, w^n, \mathbf{w}^n, \theta^n, \tag{73}$$

which represent the Faedo–Galerkin approximations of the respective functions ρ, u, $\mathbf{V}$, w, $\mathbf{w}$ and θ. These approximations can be iteratively refined to converge to the exact solution as n increases.

The Faedo–Galerkin method offers a structured way to approximate solutions for complex systems of partial differential equations, and the existence of such approximate solutions is guaranteed by the method's general theoretical framework. For a detailed exposition of the Faedo–Galerkin method in the context of abstract problems, we refer the reader to [41].

To construct the approximation space, we employ sine and cosine basis functions. We define the approximations u^n, $\mathbf{V}^n$, w^n, $\mathbf{w}^n$, θ^n as follows:

$$u^n(x,t) = \sum_{i=1}^{n} u_i^n(t)\sin(\pi i x), \quad \mathbf{V}^n(x,t) = \sum_{i=1}^{n} \mathbf{V}_i^n(t)\sin(\pi i x), \tag{74}$$

$$w^n(x,t) = \sum_{i=1}^{n} w_i^n(t)\sin(\pi i x), \quad \mathbf{w}^n(x,t) = \sum_{i=1}^{n} \mathbf{w}_i^n(t)\sin(\pi i x), \tag{75}$$

$$\theta^n(x,t) = \sum_{j=0}^{n} \theta_j^n(t)\cos(\pi j x). \tag{76}$$

These trigonometric bases are selected for their compatibility with the imposed homogeneous boundary conditions. Specifically, sine functions naturally satisfy the zero-value boundary conditions required for the velocity u, microrotation w, and the vector fields $\mathbf{V}$ and $\mathbf{w}$, ensuring that the boundary conditions

$$u^n(0,t) = u^n(1,t) = 0, \quad \mathbf{V}^n(0,t) = \mathbf{V}^n(1,t) = \mathbf{0}, \tag{77}$$

$$w^n(0,t) = w^n(1,t) = 0, \quad \mathbf{w}^n(0,t) = \mathbf{w}^n(1,t) = \mathbf{0}, \tag{78}$$

are satisfied. Conversely, the temperature θ adheres to Neumann boundary conditions, which are naturally accommodated by cosine functions with zero derivative at the boundaries:

$$\partial_x\theta^n(0,t) = \partial_x\theta^n(1,t) = 0, \tag{79}$$

in accordance with the original problem's boundary conditions.

Please note that boundary conditions for the density ρ are not explicitly prescribed, as they are influenced by non-zero fluxes and variations at domain boundaries. Representing ρ with sine or cosine functions would not accurately capture its boundary behavior and could introduce significant inaccuracies. Thus, ρ is treated as a primary variable and directly incorporated into the numerical scheme without spectral expansion. The approximation ρ^n of the density function ρ is determined by solving the initial value problem:

$$\partial_t\rho^n + L^{-1}(\rho^n)^2\partial_x u^n = 0, \tag{80}$$

$$\rho^n(x,0) = \rho_0(x). \tag{81}$$

Rewriting Equation (80) as

$$\partial_t\left(\frac{1}{\rho^n}\right) = L^{-1}\partial_x u^n, \tag{82}$$

we find that the solution to the initial problem (80) and (81) can be expressed as:

$$\rho^n(x,t) = \frac{L\rho_0(x)}{L + \rho_0(x)\int_0^t \partial_x u^n(x,\tau)d\tau}. \tag{83}$$

The approximation $\mathbf{h}^n$ of the function $\mathbf{h}$ from (55) is defined as:

$$\mathbf{h}^n(x,t) = \frac{\mathbf{a}(t)}{A}\int_0^x \frac{dy}{\rho^n(y,t)}. \tag{84}$$

To determine the approximate functions (74)–(76), we need to calculate their coefficients:

$$u_1^n(t),\ldots,u_n^n(t),\mathbf{V}_1^n(t),\ldots,\mathbf{V}_n^n(t),w_1^n(t),\ldots,w_n^n(t),\mathbf{w}_1^n(t),\ldots,\mathbf{w}_n^n(t),\theta_0^n(t),\ldots,\theta_n^n(t). \tag{85}$$

These coefficients are unknown smooth functions, which are determined using the Faedo–Galerkin approach. According to the Faedo–Galerkin method applied to the system (60)–(65), these functions satisfy the following Cauchy problem:

$$\dot{u}_i^n(t) = 2\int_0^1 \left[-L^{-1}R\partial_x\left((\rho^n)^p\theta^n\right) + L^{-2}(\lambda+2\mu)\partial_x(\rho^n\partial_x u^n)\right]\sin(\pi i x)dx, \tag{86}$$

$$\dot{\mathbf{V}}_i^n(t) = 2\int_0^1 \left[L^{-2}(\mu+\mu_r)\partial_x(\rho^n\partial_x\mathbf{V}^n) + 2L^{-1}\mu_r\nabla\times\mathbf{w}^n - \partial_t\mathbf{h}^n\right]\sin(\pi i x)dx, \tag{87}$$

$$\dot{w}_i^n(t) = 2\int_0^1 \left[\frac{c_0+2c_d}{L^2 j_I}\partial_x(\rho^n\partial_x w^n) - 4\frac{\mu_r}{j_I}\frac{w^n}{\rho^n}\right]\sin(\pi i x)dx, \tag{88}$$

$$\begin{aligned}\dot{\mathbf{w}}_i^n(t) = 2\int_0^1 \Bigg[&\frac{c_d+c_a}{L^2 j_I}\partial_x(\rho^n\partial_x\mathbf{w}^n) - \frac{4\mu_r}{j_I}\frac{\mathbf{w}^n}{\rho^n} + 2\frac{\mu_r}{Lj_I}\nabla\times\mathbf{V}^n\\ &+2\frac{\mu_r}{Lj_I}\nabla\times\mathbf{h}^n\Bigg]\sin(\pi i x)dx,\end{aligned} \tag{89}$$

$$\begin{aligned}\dot{\theta}_k^n(t) = \lambda_k\int_0^1 \Bigg[&\frac{k}{L^2c_v}\partial_x(\rho^n\partial_x\theta^n) - \frac{R}{Lc_v}(\rho^n)^p\theta^n\partial_x u^n + \frac{\lambda+2\mu}{L^2c_v}\rho^n(\partial_x u^n)^2\\ &+\frac{\mu+\mu_r}{L^2c_v}\rho^n|\partial_x\mathbf{V}^n|^2 + 2\frac{\mu+\mu_r}{L^2c_v}\rho^n\partial_x\mathbf{V}^n\partial_x\mathbf{h}^n + \frac{\mu+\mu_r}{L^2c_v}\rho^n|\partial_x\mathbf{h}^n|^2\\ &+4\frac{\mu_r}{c_v}\frac{(w^n)^2}{\rho^n} + 4\frac{\mu_r}{c_v}\frac{|\mathbf{w}^n|^2}{\rho^n} - 4\frac{\mu_r}{Lc_v}(\nabla\times\mathbf{V}^n)\cdot\mathbf{w}^n - 4\frac{\mu_r}{Lc_v}(\nabla\times\mathbf{h}^n)\cdot\mathbf{w}^n\\ &+\frac{c_0+2c_d}{L^2c_v}\rho^n(\partial_x w^n)^2 + \frac{c_d+c_a}{L^2c_v}\rho^n|\partial_x\mathbf{w}^n|^2\Bigg]\cos(\pi k x)dx,\end{aligned} \tag{90}$$

with the initial conditions

$$u_i^n(0) = 2\int_0^1 u_0(x)\sin(\pi i x)dx, \quad \mathbf{V}_i^n(0) = 2\int_0^1 \mathbf{V}_0(x)\sin(\pi i x)dx, \tag{91}$$

$$w_i^n(0) = 2\int_0^1 w_0(x)\sin(\pi i x)dx, \quad \mathbf{w}_i^n(0) = 2\int_0^1 \mathbf{w}_0(x)\sin(\pi i x)dx, \tag{92}$$

$$\theta_k^n(0) = \lambda_k\int_0^1 \theta_0(x)\cos(\pi k x)dx, \tag{93}$$

for $i = 1, \ldots, n$, $k = 0, \ldots, n$. In Equations (90) and (93), $\lambda_0 = 1$ and $\lambda_k = 2, k \geq 1$. These initial conditions (91)–(93) represent the Fourier coefficients of the initial functions $\rho_0, u_0, \mathbf{V}_0, w_0, \mathbf{w}_0$ and θ_0, respectively.

To determine the approximating function ρ^n, we substitute (74) into Equation (83) to obtain:

$$\rho^n(x,t) = \frac{L\rho_0(x)}{L + \rho_0(x)\sum_{i=1}^{n} z_i^n(t) i\pi \cos(\pi i x)}, \tag{94}$$

where the functions $z_i^n(t)$ are given by

$$z_i^n(t) = \int_0^t u_i^n(\tau)d\tau, \quad i = 1, \ldots, n. \tag{95}$$

Thus, $z_i^n(t)$ for $i = 1, \ldots, n$ satisfy the following Cauchy problem:

$$\dot{z}_i^n(t) = u_i^n, \quad z_i^n(0) = 0. \tag{96}$$

The Cauchy problem defined by Equations (86)–(93) can be expanded to include (96). The functions on the right-hand side of Equations (86) through (93) and (96) satisfy the conditions of the Cauchy-Picard theorem, ensuring that for each $n \in \mathbf{N}$, there exists an interval $[0, T_n]$ within which the initial value problem has a unique solution. Thus, the approximate solutions (73) to the problem (60)–(72), as represented by Equations (74)–(76) and (83), exist on the domain $[0,1] \times [0, T_n]$.

To represent the solutions in Eulerian coordinates, we approximate the spatial position using Equation (39) as follows:

$$\xi^n(x,t) = \xi_0(x) + \int_0^t u^n(\tau)d\tau, \quad \xi_0(x) = \eta^{-1}(Lx). \tag{97}$$

Substituting from Equation (74), we find:

$$\xi^n(x,t) = \xi_0(x) + \sum_{i=1}^{n} z_i^n(t)\sin(\pi i x). \tag{98}$$

Furthermore, since u^n is a sufficiently smooth function, Equation (83) implies that the density function ρ^n is continuous over the domain $[0,1] \times [0, T_n]$ and satisfies:

$$\rho^n(x,0) = \rho_0(x) \geq m > 0, \tag{99}$$

where m is the constant defined in (37). This allows us to select T_n such that:

$$\rho^n(x,t) > 0 \tag{100}$$

holds for all $(x,t) \in [0,1] \times [0, T_n]$.

Based on the results in [37], we can expect that, under suitable initial and boundary conditions, the sequence of approximate solutions converges to the true solution within the domain $[0,1] \times [0, T_0]$, where $T_0 > 0$ is sufficiently small. Building on these findings in [37], we anticipate that, alongside property (100), the approximate temperature solutions satisfy:

$$\theta^n(x,t) > 0 \tag{101}$$

for all $(x,t) \in [0,1] \times [0, T_n]$, assuming additionally that:

$$\theta_0(x) \geq m \tag{102}$$

on $(0,1)$. The conditions (37) and (102) are physically justified, ensuring that initial density and temperature are bounded below by a positive constant m. Properties (100) and (101)

thus guarantee that the approximate solutions preserve positivity, maintaining the physical realism of the model by preventing non-physical negative values, which could otherwise compromise the validity of simulation results.

4. Finite-Difference Approximations

The second approach we employ to obtain the numerical solution of (40)–(52) is based on finite-difference approximation. For this system, the method is efficient as it does not require homogenization of boundary conditions or variable transformations. Instead, the numerical approximation operates directly on the original system. Careful discretization is essential, however, to maintain the physical consistency of the variables and ensure system stability.

The finite-difference scheme proposed here uses a semi-discrete approach, performing spatial discretization while keeping the time variable continuous. The spatial discretization employs a staggered grid, where different variables are defined at specific locations within the computational domain. This technique enhances the accuracy and stability of finite-difference schemes, particularly for fluid dynamics problems and other systems governed by partial differential equations.

For the chosen number N of the spatial discretization cells, we denote its size by $h = \frac{1}{N}$. The one-dimensional staggered grid is defined with the cell centers and cell edges. The cell centers are denoted by $x_j = jh$, where $j \in \left\{\frac{1}{2}, \ldots, N - \frac{1}{2}\right\}$ and the cell edges by $x_k = kh$, with $k \in \{0, 1, \ldots, N\}$.

We define the following functions approximating the solution at the corresponding grid points:

$$\rho_j(t), \theta_j(t), \quad j = \frac{1}{2}, \ldots, N - \frac{1}{2},$$

and

$$u_k(t), \mathbf{u}_k(t), w_k(t), \mathbf{w}_k(t), \quad k = 0, 1, \ldots, N,$$

where $g_l(t) \approx g(x_l, t)$, for $g \in \{\rho, u, \mathbf{u}, w, \mathbf{w}, \theta\}$, and $l = j$ or $l = k$. Please note that the variables are not all defined at the same grid points. Instead, they are offset (staggered) relative to one another. Specifically, the functions representing pressure and density are located at the centers of grid cells, while those representing velocity and microrotation velocity components are defined at the cell edges. This layout helps prevent numerical instabilities and enables a more physically accurate coupling between variables. The convergence of similar numerical schemes has been established in previous works [33,34].

The functions $\rho_j(t)$, $u_k(t)$, $\mathbf{u}_k(t)$, $w_k(t)$, $\mathbf{w}_k(t)$, and $\theta_j(t)$ are obtained by solving an ordinary differential equation system derived by applying the finite-difference approximations on the proposed spatial discretization to the problem (40)–(52). More precisely, the partial derivatives are approximated using centered finite differences of the form, i.e.,

$$\frac{\partial g(x_l, t)}{\partial x} \approx \delta_l g(t) = \frac{g_{l+\frac{1}{2}}(t) - g_{l-\frac{1}{2}}(t)}{h}, \tag{103}$$

for $l = j$ or $l = k$. Observe that the proposed discretization (103) involves the approximation of the derivatives at the centers of the cells, as well as at the cell edges, making use of a staggered grid arrangement. Finally, this leads to the following system:

$$\dot{\rho}_j = -L^{-1}\rho_j^2\,\delta_j u, \tag{104}$$

$$\dot{u}_k = -L^{-1}R\,\delta_k(\rho^p\theta) + L^{-2}(\lambda + 2\mu)\,\delta_k(\rho\,\delta u), \tag{105}$$

$$\dot{\mathbf{u}}_k = L^{-2}(\mu + \mu_r)\,\delta_k(\rho\,\delta\mathbf{u}) + 2L^{-1}\mu_r\nabla\times\mathbf{w}_k, \tag{106}$$

$$j_I\dot{w}_k = L^{-2}(c_0 + 2c_d)\,\delta_k(\rho\,\delta w) - 4\mu_r\frac{w_k}{\rho_k}, \tag{107}$$

$$j_I \dot{\mathbf{w}}_k = L^{-2}(c_d + c_a)\,\delta_k(\rho\,\delta\mathbf{w}) - \frac{4\mu_r}{\rho_k}\mathbf{w}_k + 2L^{-1}\mu_r \nabla \times \mathbf{u}_k, \tag{108}$$

$$\begin{aligned} c_v\dot{\theta}_k = {} & L^{-2}k_\theta\delta_j(\rho\delta\theta) - L^{-1}R\rho_j^p\theta_j\delta_j u + L^{-2}(\lambda+2\mu)\rho(\delta_j u)^2 \\ & + L^{-2}(\mu+\mu_r)\rho|\delta_j\mathbf{u}|^2 + 4\mu_r\frac{w_j^2}{\rho_j} + 4\mu_r\frac{|\mathbf{w}_j|^2}{\rho_j} - 4L^{-1}\mu_r(\nabla\times\mathbf{u}_j)\cdot\mathbf{w}_j + \\ & L^{-2}(c_0+2c_d)\rho_j(\delta_j w)^2 + L^{-2}(c_d+c_a)\rho|\delta_j\mathbf{w}|^2. \end{aligned} \tag{109}$$

for $j = \frac{1}{2}, \ldots, N-\frac{1}{2}$ and $k = 1, \ldots, N-1$. The initial conditions for the approximate functions are computed by evaluating the initial functions at the appropriate locations of the grid cells. The solutions of this Cauchy problem are the approximate functions $\rho_j(t)$, $u_k(t)$, $\mathbf{u}_k(t)$, $w_k(t)$, $\mathbf{w}_k(t)$, and $\theta_j(t)$, $j = \frac{1}{2}, \ldots, N-\frac{1}{2}$ and $k = 1, \ldots, N-1$.

Please note that the resulting system does not include differential equations for the boundary values

$$u_0(t), \mathbf{u}_0(t), w_0(t), \mathbf{w}_0(t), \delta\theta_0(t), u_N(t), \mathbf{u}_N(t), w_N(t), \mathbf{w}_N(t), \delta\theta_N(t),$$

although these values appear on the right-hand side of the equations. Instead, these values are directly specified by the boundary conditions (50)–(52). The use of a staggered grid simplifies the discretization of boundary conditions, making the method more physically consistent with the problem at hand.

In certain equations, values of functions defined at cell centers are needed at cell edges, and vice versa. In such cases, a simple averaging of neighboring values is used to estimate the required values at these locations.

In order to present the numerical results in Eulerian coordinates, similarly as in the Faedo–Galerkin method, we add the additional equations to the system (104)–(109) through which we compute the approximations of the spatial point positions in Eulerian framework. From the expression (39), it is clear that the spatial position $\xi(x,t)$ is the solution of the differential equation:

$$\frac{d\xi}{dt} = u(x,t) \tag{110}$$

with the initial condition $\xi(x,0) = \eta^{-1}(Lx)$. For the considered discretization of the cell edges x_k, we obtain from (110) the differential equations for the spatial positions of these cell edges $\xi_k(t) \approx \xi(x_k,t)$:

$$\dot{\xi}_k = u_k, \quad k = 0, 1, \ldots, N. \tag{111}$$

The solution of (111) gives the approximations of the Eulerian coordinates of the cell edges at time t.

Similarly to the Faedo–Galerkin approach, we can conclude that for the obtained system of ODEs (104)–(109) and (110), the conditions of the Cauchy-Picard theorem are satisfied. Therefore, this system has a solution on some interval $[0,T]$, $T > 0$. It can also be concluded that if the initial functions ρ_0 and θ_0 are bounded from below, the same will hold for the approximation functions $\rho_j(t)$ and $\theta_j(t)$, $j = \frac{1}{2}, \ldots, N-\frac{1}{2}$, on $[0,T_0]$ for at least some sufficiently small $T_0 > 0$ so that the solutions remain physical meaningful.

We emphasize once again that a key aspect of our approach is the use of a staggered grid layout, which ensures that the spatial discretization accurately captures interactions between physical quantities and allows for precise handling of boundary conditions. This setup minimizes the likelihood of spurious oscillations or numerical artifacts, significantly enhancing the stability of the numerical scheme. Compared to the Faedo–Galerkin method, this approach allows for the direct implementation of boundary conditions without requiring homogenization or the introduction of new variables. The efficiency of both methods will be compared in the examples in the next chapter, though the finite-difference method is expected to be more efficient due to its lower computational demands.

5. Numerical Experiments

In this section, we perform numerical simulations of the problem of micropolar fluid flow described by Equations (40)–(52). This system involves complex physical dependencies between variables that arise from the conservation laws. To set up a concrete test example, it is sufficient to specify the physical parameters, define the initial conditions for all variables, and a boundary condition that describes the motion of the upper plate.

Then, the proposed numerical methods, the Faedo–Galerkin method and the finite-difference method, are applied to solve the system of Equations (40)–(52). In both proposed approximation approaches, we obtained a system of ordinary differential equations that needs to be solved.

In fact, in the Faedo–Galerkin method, it is first necessary to calculate the values of the integrals that appear on the right-hand side of Equations (86)–(90). For this purpose, numerical integration will be used, specifically Gauss-Legendre quadrature formulas. After testing quadrature formulas of various orders, the quadrature formulas of order 10 were selected. The nodes and weights of the quadrature formula were determined using ready-to-use *Matlab* function.

In both approaches, the remaining task is to find the solutions of the ODE system, which can be written as

$$\dot{\mathbf{U}}(t) = \mathbf{F}(\mathbf{U}(t)),$$

where $\mathbf{U}$ denotes the vector of variables and $\mathbf{F}$ represents the right-hand side of the derived systems. With the appropriate initial conditions, the temporal integration of this system can be performed using a numerical method for solving ordinary differential equations systems. The strong stability-preserving (SSP) third-order explicit Runge–Kutta method [42] proved to be a good choice in all the considered examples. The main advantage of SSP methods is that they ensure that the stability properties of a numerical scheme are preserved under time integration. They were initially motivated by the need to handle non-linearities in conservation laws and are designed to prevent spurious oscillations in regions of steep gradients or discontinuities. If the spatial discretization is stable for a forward Euler step, then an SSP Runge–Kutta method will keep that stability property even with multiple steps [42].

In the following, we examine the behavior of solutions for selected problems, focusing on several aspects. First, we analyze the model itself: the influence of the parameter p in the real gas model and the effects of various physical parameters on solution behavior. We also investigate convergence to the stationary solution. Another focus is the performance of the numerical methods. By comparing solutions obtained with different methods, we partially validate the results. Additionally, we examine the stability of solutions and convergence of each method and the influence of model parameters on them. Efficiency is also an important aspect of these methods and is evaluated in this analysis.

5.1. Comparison of the Numerical Methods and the Influence of the Parameter p

In the manuscript, we analyze two practical examples to evaluate the performance of the numerical methods. In both examples, we use the same physical parameters for the system. Since, to our knowledge, no experimental results are covering this area, parameters are selected arbitrarily while ensuring they satisfy constraints (9) and (10).

The following physical parameters of the system are set to $L = 1\,[\frac{kg}{m^2}]$, $j_I = 1\,[\frac{kg}{ms}]$, $R = 1\,[\frac{J}{kgK}]$, $k_\theta = 0.024\,[K]$. For the coefficients of viscosity and microrotation viscosity, we take in the first case:

$$\begin{aligned} \text{Case (a):} \quad & c_d = c_0 = c_v = 10^{-3}\,[\tfrac{kg}{ms}],\ c_a = 0\,[\tfrac{kg}{ms}],\ \lambda = -2\cdot 10^{-3}\,[\tfrac{kg}{ms}], \\ & \mu_r = 10^{-3}\,[\tfrac{kg}{ms}],\ \text{and}\ \mu = 3\cdot 10^{-3}\,[\tfrac{kg}{ms}], \end{aligned}$$

while in Case (b) we take these coefficients hundred times larger, i.e.,

$$\begin{aligned}\text{Case (b):}\quad & c_d = c_0 = c_v = 10^{-1}\,[\tfrac{kg}{ms}],\ c_a = 0\,[\tfrac{kg}{ms}],\ \lambda = -2\cdot 10^{-1}\,[\tfrac{kg}{ms}],\\ & \mu_r = 10^{-1}\,[\tfrac{kg}{ms}],\ \text{and}\ \mu = 3\cdot 10^{-1}\,[\tfrac{kg}{ms}],\end{aligned}$$

to examine their effect on the problem solution.

5.1.1. Example 1

We assume here that the initial conditions are defined in mass Lagrangian coordinates. More precisely, we seek the solution to the problem (40)–(52) with the following initial conditions:

$$\begin{aligned}&\rho_0(x) = 1,\\ &u_0(x) = \sin(\pi x), \quad \mathbf{u}_0(x) = \sin(\pi x)(0,1,1),\\ &w_0(x) = \sin(2\pi x), \quad \mathbf{w}_0(x) = \sin(2\pi x)(0,1,1),\\ &\theta_0(x) = 2+\cos(\pi x),\end{aligned} \tag{112}$$

The boundary conditions are defined by (50)–(52). We assume that the upper plate moves according to the law described by the function:

$$\mathbf{a}(t) = 0.5\sin(\pi t)(0,1,1). \tag{113}$$

Using the previously defined physical parameters, the problem is completely defined.

In this example, smooth functions with a finite number of harmonics in their Fourier expansion are selected as initial conditions. This choice is well-suited for the Faedo–Galerkin method, as such initial conditions are expected to demonstrate favorable numerical properties. Furthermore, the initial density is chosen to simplify the return to Eulerian coordinates, reducing potential computational complexity. Within this example, we investigate two subcases: in the first, the viscosity coefficients are of smaller magnitude, making the system closer to a hyperbolic regime; in the second, the viscosity coefficients are of larger magnitude, emphasizing the parabolic nature of the system in numerical terms.

In the calculations, the finite-difference numerical method with $N = 64$ spatial cells and the Faedo–Galerkin method with $n = 20$ expansion terms were used. The time step used for temporal discretization was adjusted so that the stability properties are satisfied, and we set it here to $\Delta t = 10^{-3}$ for both methods.

In the solution representation, Eulerian coordinates are used. Since, in these examples, the initial density is given in mass Lagrangian coordinates, we need the transformation from mass Lagrangian to Eulerian coordinates. It follows from (35), (36) and (39), that $\frac{d\xi_0}{dx} = \frac{L}{\rho_0(x)}$, which after integrating over $[0,x]$ gives the initial position in Eulerian coordinates, i.e., $\xi_0(x) = L\int_0^x \frac{dy}{\rho_0(y)}$. For $x = 1$, we obtain $h = \xi_0(1) = L\cdot A$, where A is defined in (57). Thus, instead of specifying the width h between the plates, the parameter L is prescribed, and we take here $L = \frac{1}{A}$ to obtain $h = 1$. The positions of the discretization points at time t in Eulerian coordinates are determined using (98) in the Faedo–Galerkin method or by solving Equation (110) in the finite-difference method. The evolution of discretization points $\xi(x_k,t), k = 0,\ldots,N$, $N = 64$ representing their spatial positions in Eulerian coordinates are presented in Figure 1.

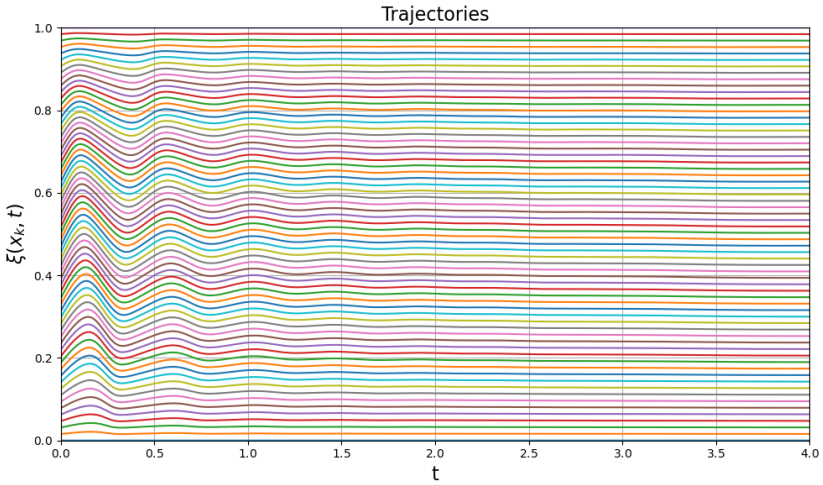


Figure 1. Example 1. Case (a) The evolution of spatial discretization positions in Eulerian coordinates.

Next, we compare the solutions obtained by both numerical methods for various values of the parameter p. This comparison helps validate the numerical solutions, as the methods are fundamentally different. Simultaneously, we investigate the influence of the parameter p on the solutions. To complete the analysis and thoroughly investigate the effects of micropolarity, the solutions obtained from the simulation of micropolar fluid flow are also compared with those derived from the equations for classical fluid flow, for which the same initial and boundary conditions are applied, with the exception of the micropolar velocity, which is set to $\omega = 0$.

Figures 2–5 display the numerical solutions for Case (a) of this example, obtained with both methods for parameter values $p \in \{1, 2, 3, 4, 5\}$, as well as for the classical fluid flow case without micropolarity, at selected time points. Figures 6–9 show the numerical solutions for larger parameter values, i.e., for Case (b).

Our observations are summarized as follows. In both cases, the influence of the parameter p on the solution is evident. Also, the comparison of solutions obtained from the classical fluid flow model with those of the micropolar flow model clearly reveals the impact of micropolarity on the solutions. Additionally, the solutions obtained by the Faedo–Galerkin method and the finite-difference method align well overall. However, oscillations in the Faedo–Galerkin solutions are noticeable in both cases, with much larger oscillations in Case (a) than in Case (b). We attribute this to the fact that, with very small viscosity and microrotational viscosity coefficients, viscosity effects become negligible, and the system approaches a hyperbolic system. It is well-known that solutions in hyperbolic systems can exhibit discontinuities, and in such cases, alternative numerical methods are often needed to accurately capture these discontinuities. With higher viscosity, the solutions are smoother, and the Faedo–Galerkin method does not produce oscillations. In this case, the solutions obtained by both methods agree even more closely.

In this example, we also investigate the efficiency of the numerical methods. In Table 1, the computation times for both methods using different computational parameters, with a final time of $t_{\max} = 10$ s, are shown. The finite-difference method with $N = 64$ points provides very stable results that match well with those obtained on a denser grid, while the computation time is significantly shorter than that of the Faedo–Galerkin method of relatively low order. From the results, it can be concluded that the finite-difference method provides a better balance between accuracy and computational efficiency than the Faedo–Galerkin method.

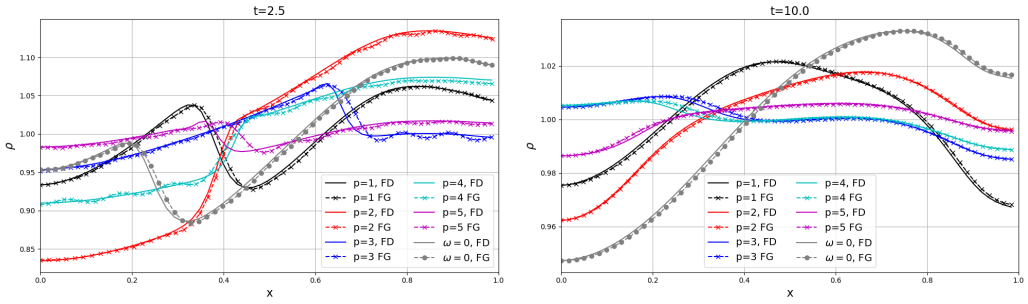


Figure 2. Example 1. Case (a) Comparison of the numerical results obtained by the finite-difference and the Faedo–Galerkin method for different p at chosen time moments—density ρ.

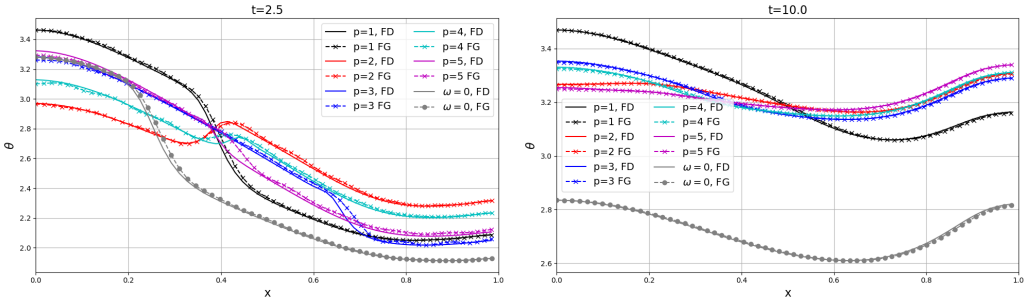


Figure 3. Example 1. Case (a) Comparison of the numerical results obtained by the finite-difference and the Faedo–Galerkin method for different p at chosen time moments—temperature θ.

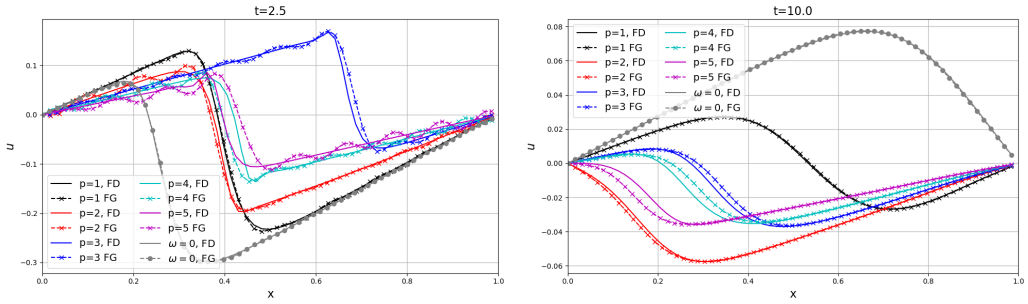


Figure 4. Example 1. Case (a) Comparison of the numerical results obtained by the finite-difference and the Faedo–Galerkin method for different p at chosen time moments—velocity u.

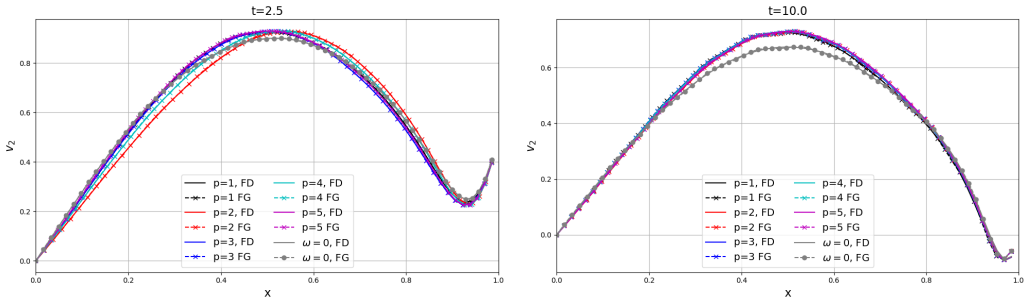


Figure 5. Example 1. Case (a) Comparison of the numerical results obtained by the finite-difference and the Faedo–Galerkin method for different p at chosen time moments—velocity v_2.

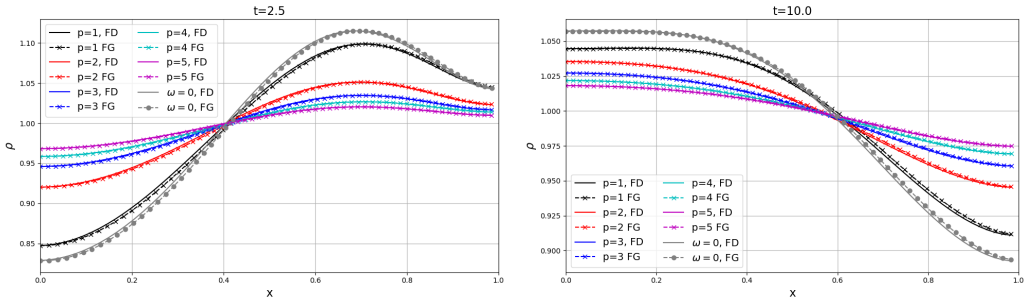


Figure 6. Example 1. Case (b) Comparison of the numerical results obtained by the finite-difference and the Faedo–Galerkin method for different p at chosen time moments—density ρ.

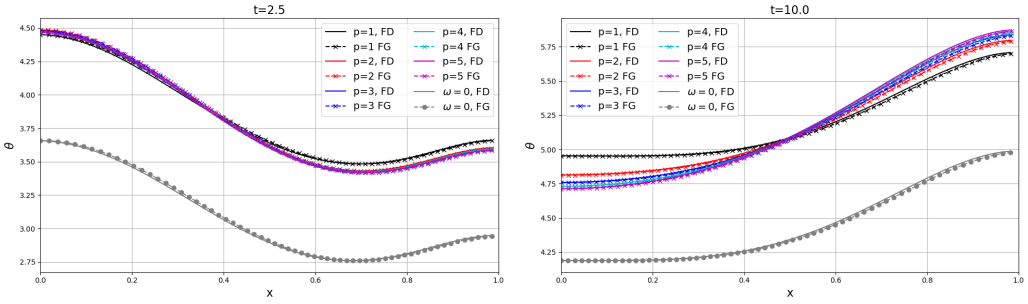


Figure 7. Example 1. Case (b) Comparison of the numerical results obtained by the finite-difference and the Faedo–Galerkin method for different p at chosen time moments—temperature θ.

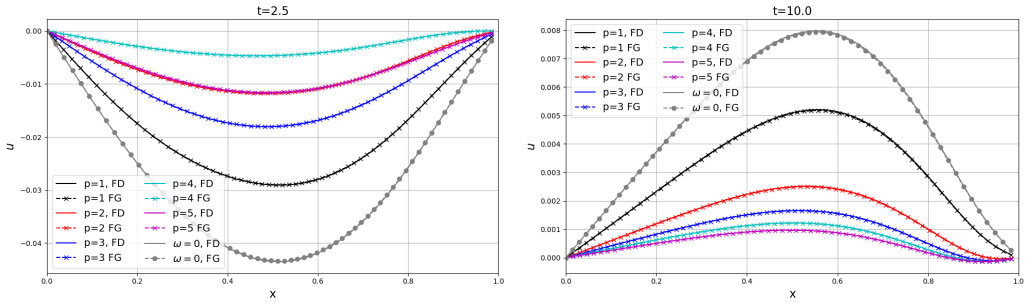


Figure 8. Example 1. Case (b) Comparison of the numerical results obtained by the finite-difference and the Faedo–Galerkin method for different p at chosen time moments—velocity u.

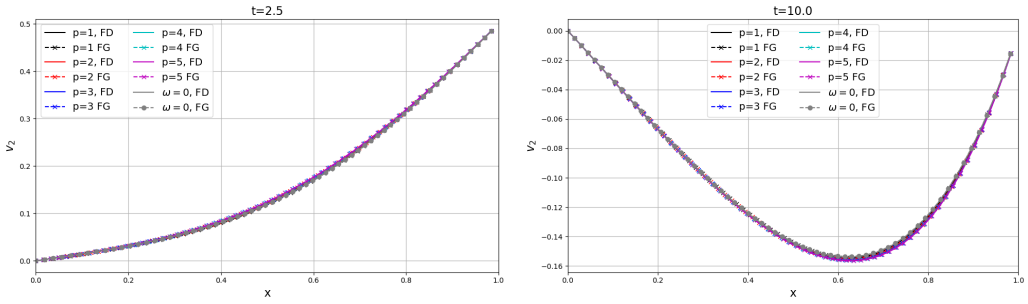


Figure 9. Example 1. Case (b) Comparison of the numerical results obtained by the finite-difference and the Faedo–Galerkin method for different p at chosen time moments—velocity v_2.

Table 1. CPU times obtained with different computational parameters. Example 1.

Numerical Scheme	CPU Time (s)
finite difference, $\Delta t = 10^{-3}$, $N = 64$	5.29
finite difference, $\Delta t = 10^{-3}$, $N = 128$	6.84
Faedo–Galerkin, $\Delta t = 10^{-3}$, $n = 5$	55.49
Faedo–Galerkin, $\Delta t = 10^{-3}$, $n = 10$	109.49
Faedo–Galerkin, $\Delta t = 10^{-3}$, $n = 20$	212.2

5.1.2. Example 2

In the second test example, we assume that the initial density is not smooth as in the previous example, i.e., we take:

$$\begin{aligned} \rho_0(x) &= 1 - (0.5 - |x - 0.5|)^2, \\ u_0(x) &= x(1-x), \quad \mathbf{u}_0(x) = x(1-x)(0,1,1), \\ w_0(x) &= x^2(1-x^2), \quad \mathbf{w}_0(x) = x^2(1-x^2)(0,1,1), \\ \theta_0(x) &= 2x^3 - 3x^2 + 2. \end{aligned} \tag{114}$$

The boundary conditions in this example are defined in the same way as in Example 1, using the velocity vector:

$$\mathbf{a}(t) = 0.5 \sin(\pi t)(0,1,1).$$

In this example, significantly more complex initial conditions are considered, involving functions with an infinite number of harmonics in their Fourier expansion, which theoretically present challenges for the Faedo–Galerkin method. Additionally, the initial density is no longer a smooth function. For this example, we focus exclusively on Case (b) with more pronounced viscosity, emphasizing parabolicity, as the goal is to explore how the complexity of initial conditions impacts the behavior of the numerical methods. As before, we compare the solutions obtained using the Faedo–Galerkin method and the finite-difference method. The purpose of the presented results is to compare the numerical methods, to investigate the influence of the parameter p, and to evaluate the effects of micropolarity since solutions from classical fluid flow simulation are also included.

In Figure 10, we can see that the numerical solution obtained using the Faedo–Galerkin method exhibits oscillations near the point where the initial function is not differentiable. This behaviour is due to the properties of the Fourier expansion near points where the function is not smooth. In the rest of the domain, the results for the density coincide quite well. On the other hand, it can be observed that the smooth functions, namely temperature and velocity, agree well across the entire domain, as shown in Figures 11–13.

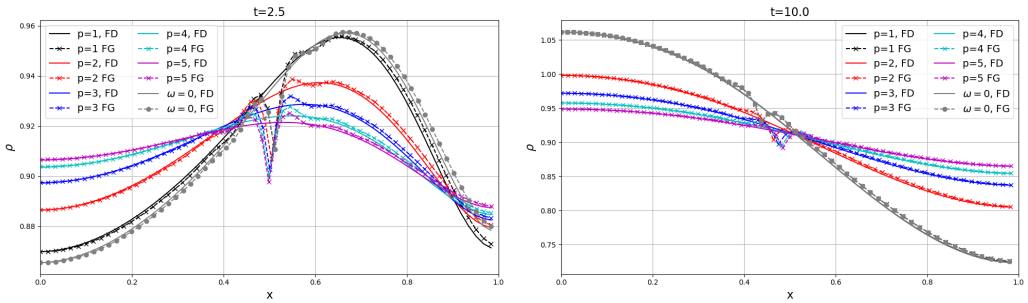


Figure 10. Example 2. Case (b) Comparison of the numerical results obtained by the finite-difference and the Faedo–Galerkin method for different p at different time moments—density ρ.

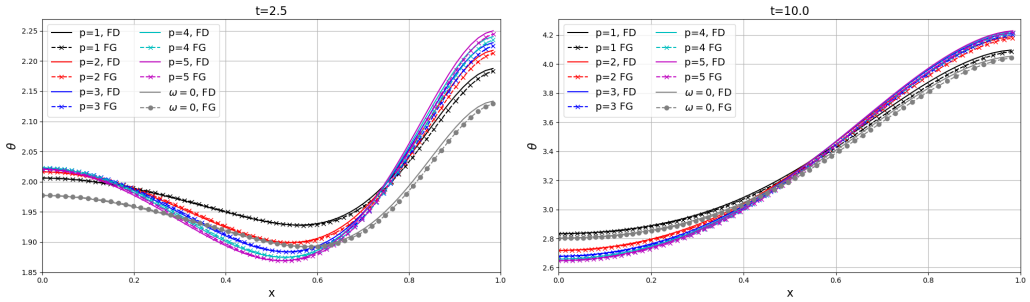


Figure 11. Example 2. Case (b) Comparison of the numerical results obtained by the finite-difference and the Faedo–Galerkin method for different p at different time moments—temperature θ.

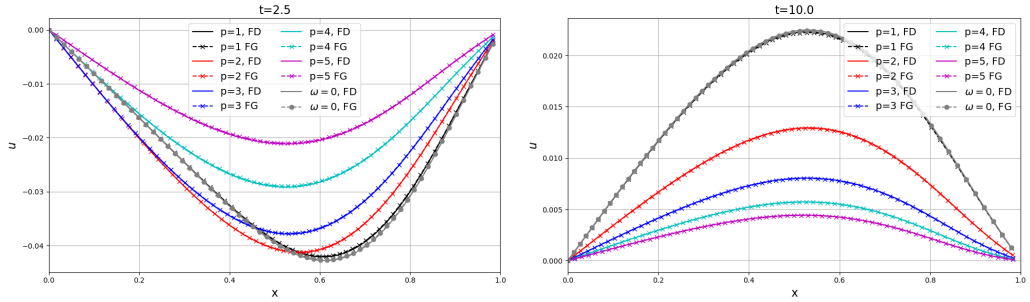


Figure 12. Example 2. Case (b) Comparison of the numerical results obtained by the finite-difference and the Faedo–Galerkin method for different p at different time moments—velocity u.

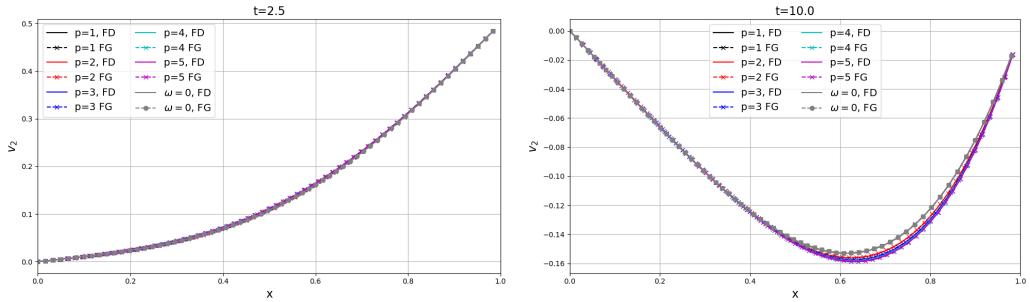


Figure 13. Example 2. Case (b) Comparison of the numerical results obtained by the finite-difference and the Faedo–Galerkin method for different p at different time moments—velocity v_2.

5.2. Numerical Convergence and Stabilization of the Solution

In the following analysis, we examine the solutions to the problems defined by the initial functions from Examples 1 and 2, assuming homogeneous boundary conditions. Thus, we assume here that the upper plate velocity is $\mathbf{a}(t) = 0$. Moreover, we take parameters as defined in Case (b).

5.2.1. Convergence of the Numerical Schemes

We study first the convergence of the numerical solutions obtained via the Faedo–Galerkin method with respect to the number of terms in the Fourier expansion. More specifically, we compute the L_∞-norm of the difference between the numerical approximations as a function of the number of terms n in the approximate solutions, where $t \in [0, 1]$.

The results are shown in Figures 14 and 15 for both test examples. The figures clearly show that the norms of these differences decrease as n increases. We plot the norms for selected variables $\phi \in \{\rho, u, w, \theta\}$ and two different values of the parameter $p \in \{1, 5\}$. As expected, this convergence is stable if the initial density function is smooth. For a non-smooth initial density, as used in Example 2, we observe larger variability in the convergence behavior (see Figure 15).

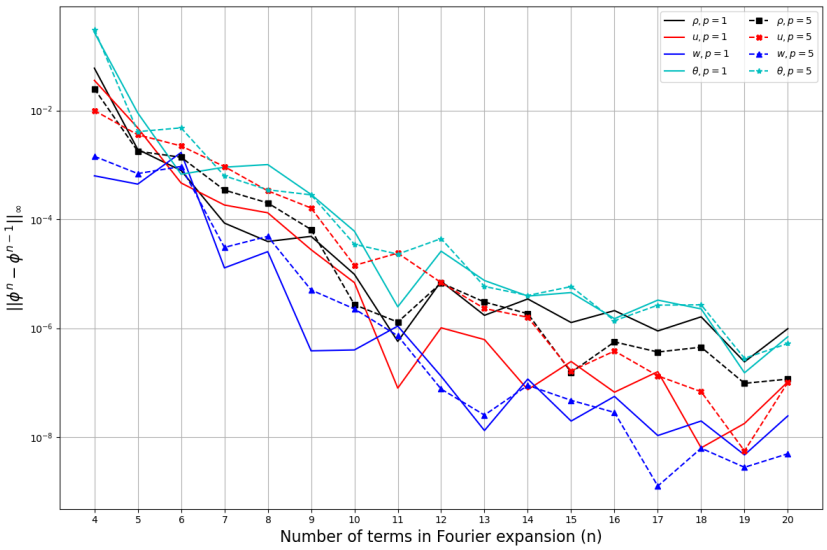


Figure 14. Example 1. Case (b) Convergence analysis of the numerical solutions obtained with the Faedo–Galerkin method.

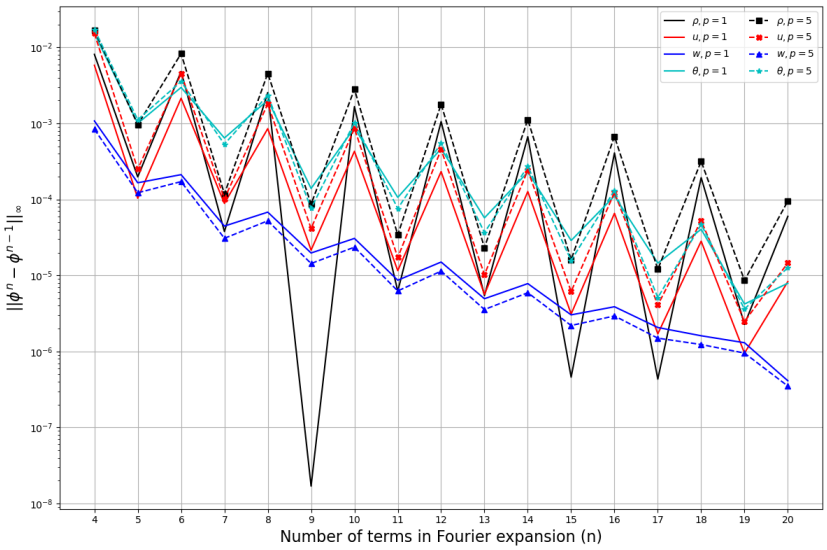


Figure 15. Example 2. Case (b) Convergence analysis of the numerical solutions obtained with the Faedo–Galerkin method.

The convergence analysis for the finite-difference method is performed as follows. Since the exact solution to the problem is unknown, we obtain a sufficiently accurate approximation of the solution using the Faedo–Galerkin method with $n = 20$ terms in the Fourier expansion and a sufficiently small value of the time step Δt, which ensures stability. We then estimate the L_1 error by calculating the difference between the solutions obtained with the Faedo–Galerkin method and the finite-difference method at the discretization points. More precisely, let ϕ^{FG} and ϕ^{FD} denote the numerical solutions obtained with the Faedo–Galerkin and finite-difference methods, respectively, where $\phi \in \{\rho, u, v_2, v_3, w, \omega_2, \omega_3, \theta\}$. The estimate of the numerical errors $E_N(\phi, t)$ associated with N discretization points, are calculated as

$$E_N(\phi, t) = \sum_{k=0}^{N} |\phi_k^{FD}(t) - \phi^{FG}(x_k, t)|h, \text{ for } \phi \in \{u, v_2, v_3, w, \omega_2, \omega_3\} \tag{115}$$

and

$$E_N(\phi,t) = \sum_{j=\frac{1}{2}}^{N-\frac{1}{2}} |\phi_j^{FD}(t) - \phi^{FG}(x_j,t)|h, \text{ for } \phi \in \{\rho,\theta\}. \tag{116}$$

Figure 16 shows the numerical errors at time $t = 1$ with respect to the number of discretization points for selected variables $\phi \in \{\rho, u, w, \theta\}$ and for two selected values $p \in \{1, 5\}$. In the analysis, we used $N = 8, 16, 32, 64, 128, 256$ discretization points and a time step small enough to ensure numerical stability. The figure illustrates that the error decreases as the number of discretization points increases. The order of accuracy, calculated as $\log_2(E_{N/2}(\phi,t)/E_N(\phi,t))$ is between 1 and 1.4 for all variables. This indicates that the spatial discretization obtained with the finite-difference method is first-order accurate, as expected.

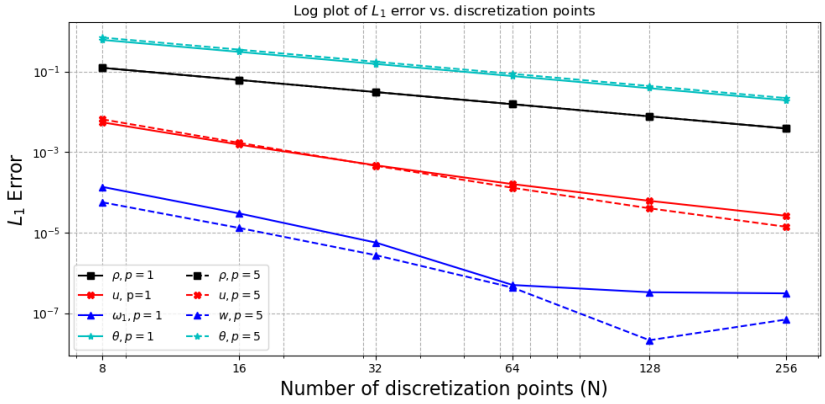


Figure 16. Example 1. Case (b) Mesh convergence analysis of the numerical solutions obtained with the finite-difference method.

5.2.2. Stabilization of the Solution

We now examine the stabilization of the solution based on the initial conditions defining both test examples. According to established theory, in similar cases, solutions can stabilize under homogeneous boundary conditions, converging toward a stationary solution. Thus, as before, we assume $\mathbf{a}(t) = 0$.

We are therefore interested in the convergence of the solutions to the stationary solution as t increases. The stabilization of the solution for some shear flow models was studied in [23,43]. For the case of a classical fluid (without micropolarity, i.e., $\boldsymbol{\omega} = 0$), but with the inclusion of the real gas state equation, an exponential stabilization of the solution for the flow between parallel plates was established in [23]. More precisely, the solutions to the problem are defined with initial functions satisfying some smoothness properties and with homogeneous boundary conditions for the velocity to converge exponentially to certain constants. It was also shown that this stabilization does not depend on the parameter p. Furthermore, in [43], the stabilization of the solution for the shear flow model of a micropolar ideal fluid developed in [39] was investigated, where it was shown that exponential stabilization holds. It was proven there that the solution $(\rho, \mathbf{v}, \boldsymbol{\omega}, \theta)$ of the problem (40)–(52) for $p = 1$, i.e., for the case of the ideal gas, converges as $t \to \infty$ to the stationary constant solution $(\rho^*, \mathbf{0}, \mathbf{0}, \theta^*)$, where

$$\rho^* = \left(\int_0^1 \frac{dx}{\rho_0(x)}\right)^{-1}, \quad \theta^* = \frac{1}{c_v}\int_0^1 \left(c_v\theta_0(x) + \frac{1}{2}\left|\mathbf{v}_0(x)\right|^2 + \frac{j_I}{2}\left|\boldsymbol{\omega}_0(x)\right|^2\right) dx, \tag{117}$$

and $|\cdot|$ denotes the vector norm. It was also shown that there exist positive constants C and γ, so that for any $t \geq 0$ the following estimate holds:

$$\left\|\frac{1}{\rho} - \frac{1}{\rho^*}\right\|^2 + \|\mathbf{v}\|^2 + \|\boldsymbol{\omega}\|^2 + \|\theta - \theta^*\|^2 \leq Ce^{-\gamma t}, \tag{118}$$

where $\|\cdot\|$ denotes H_1 norm. Based on these findings, we can hypothesize that exponential stabilization also occurs in the present cases, and we investigate this hypothesis numerically. However, a formal proof of the stabilization is beyond the scope of this paper.

For the selected test example, using Equation (117), we obtain for initial conditions of the Example 1:

$$\rho^* = 1 \text{ and } \theta^* = 3.5,$$

while from the initial conditions defining Example 2, we obtain

$$\rho^* = 0.910239 \text{ and } \theta^* = 1.588095.$$

In Figures 17 and 18, the H_1 norm of the differences between the numerical solutions obtained with the finite-difference method and the stationary solutions for different values of the parameter p is presented. In both cases and for all values of p, the exponential decay is clearly visible. In addition, the exponential decay is faster for larger values of p for the variable ρ, while it is slower for the variable θ. For the variables v and ω, the differences in the convergence decay are not visible in the figures shown. We performed further numerical investigations of the long-term behavior of the solution for different test cases, and in all cases, the results confirmed the stabilization of the solution according to Equation (117).

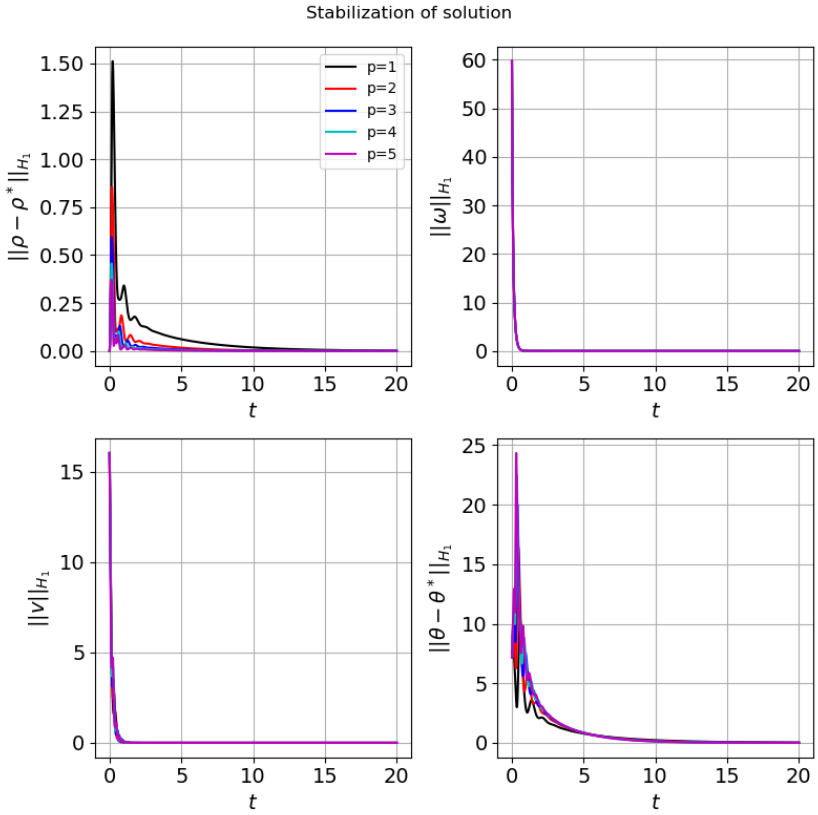


Figure 17. Example 1. Stabilization of the solution.

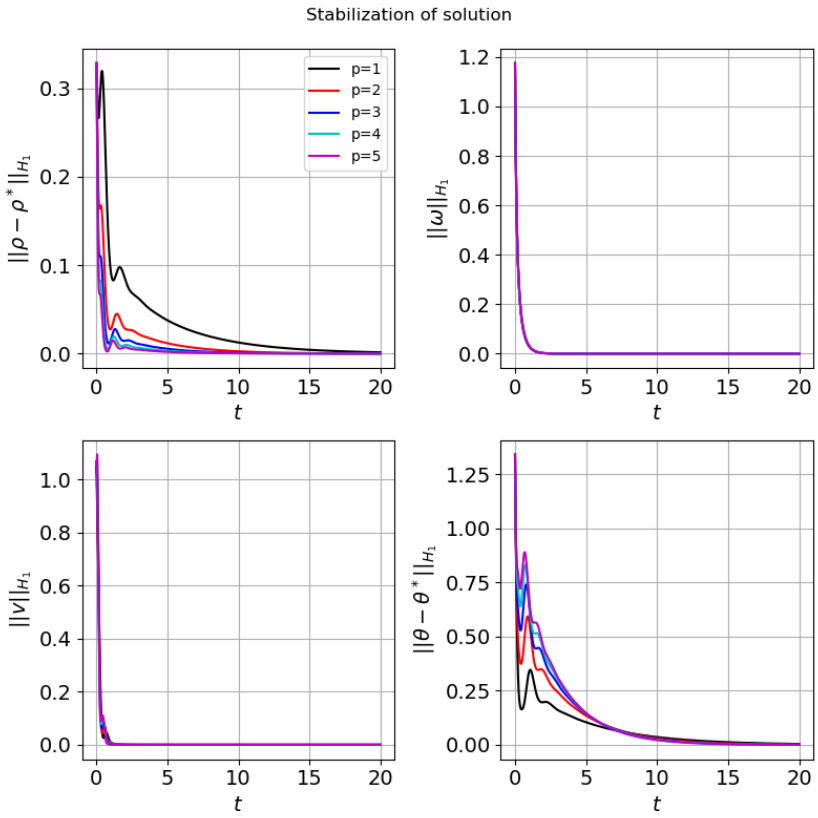


Figure 18. Example 2. Stabilization of the solution.

6. Research Contributions and Implications

This research presents two significant contributions to the existing literature. First, it develops a physically consistent model that integrates shear flow for compressible micropolar fluids with one-dimensional micropolar real gas dynamics, expanding the scope of previous studies that treated these phenomena separately. Second, it provides a detailed analysis of the strengths and weaknesses of two numerical methods—Faedo–Galerkin and finite difference—when applied to this unified model.

The study uniquely examines the influence of pressure exponents, micropolarity, and, for the first time, the implications of weak viscosity, which approximates hyperbolic systems. This previously unexplored regime reveals new insights into system behavior under such conditions. Furthermore, the numerical analysis highlights key trade-offs: while the Faedo–Galerkin method excels in establishing theoretical properties such as existence and convergence, its computational complexity and execution time, noted in prior studies, pose significant challenges for practical applications. In contrast, the finite-difference method demonstrates computational efficiency and adaptability. This dominance of finite-difference methods, frequently observed in related research, is corroborated by the results of this study, which show its superior applicability in solving hyperbolic-like systems efficiently and reliably.

These findings not only reinforce the practical advantages of finite-difference methods but also provide a robust foundation for selecting appropriate numerical approaches in future research on similar complex fluid systems. The insights gained contribute to guiding future studies in optimizing numerical techniques to balance theoretical rigor with computational feasibility.

7. Conclusions

In this work, we have investigated the behavior of a compressible micropolar fluid model in shear flow with real gas effects using two distinct numerical methods: the

Faedo–Galerkin method and the finite-difference method. Our objective was to develop stable and accurate numerical solutions that faithfully reflect the dynamics of the system under various initial conditions and parameter values.

Starting from a well-defined system of governing equations with appropriate initial and boundary conditions, we explored how factors such as viscosity, microrotation, and real gas effects impact system behavior. By comparing the numerical solutions derived from both methods across different values of the parameter p, we observed consistent solutions between the methods, with the finite-difference approach demonstrating advantages in computational speed and stability.

Another key aspect of this study is the detailed evaluation of the numerical methods employed. While the Faedo–Galerkin method is theoretically rigorous and ensures high accuracy under sufficiently smooth initial conditions, it exhibits computational inefficiencies and sensitivity to non-smooth inputs. These limitations align with prior observations in the literature, emphasizing the method's suitability primarily for theoretical validation rather than practical applications. In contrast, the finite-difference method demonstrated robust performance across a wide range of parameter values and initial conditions, excelling in both computational efficiency and stability. Its consistent dominance in similar contexts, as noted in earlier studies, was reaffirmed here, particularly for problems approaching hyperbolic regimes where lower viscosity coefficients amplify challenges.

Despite the contributions of this work, certain limitations inherent to the model should be acknowledged. The framework is specifically developed for shear flow conditions, which imposes restrictions on its applicability to more generalized or multi-dimensional flow scenarios. The assumption of shear flow simplifies the governing equations but may overlook important interactions present in more complex fluid dynamics systems. Additionally, the model's reliance on specific parameterizations, such as the microrotation and viscosity coefficients, may limit its predictive capability when these parameters deviate significantly from the considered ranges. These constraints highlight the need for future work to extend the model to broader settings, such as fully three-dimensional or non-homogeneous flow environments, where additional phenomena like turbulence or secondary flows might play a significant role.

A crucial experimental observation was the preservation of positivity for density and temperature throughout the simulations. This finding affirms the physical realism and internal consistency of both the numerical methods and the model itself, validating that each approach adheres to the fundamental requirements of the physical system.

Our analysis further highlighted the significant influence of the parameter p on the solution, providing strong justification for incorporating a real gas model in cases where ideal gas assumptions may fall short. The Faedo–Galerkin method proved sensitive to initial conditions lacking sufficient smoothness, leading to oscillations that may limit its application in certain settings. Additionally, we observed challenges related to stability when approaching a hyperbolic regime, as lower viscosity coefficients reduced the stabilizing effects of diffusion and increased sensitivity to numerical instabilities.

To evaluate the long-term behavior of the solutions, we examined the stabilization of the system. Building on established theoretical results, we hypothesized that exponential stabilization would occur, and our numerical results confirmed this hypothesis. Both methods exhibited convergence toward the stationary solution with exponential decay, with the convergence rate faster for higher values of p in the density variable, while slower for temperature. The success of achieving stabilization numerically supports the reliability of both methods in capturing the long-term behavior of the model.

Overall, these results demonstrate that both numerical approaches yield valuable insights into the behavior of compressible micropolar fluids in shear flow conditions, with the finite-difference method particularly distinguished by its computational efficiency. Our findings justify the use of a real gas model and underscore the complex interplay of model parameters, suggesting directions for further study. Future work might include formal proofs of stabilization, extensions of the model to multi-dimensional or more intricate flow

conditions, and more sophisticated treatment of initial conditions in methods sensitive to smoothness. Such research holds the potential to deepen the theoretical and numerical understanding of micropolar fluid dynamics, with applications in simulations for industrial processes and other domains where micropolarity and compressibility are critical factors.

Author Contributions: Conceptualization, N.Č. and I.D.; methodology, N.Č. and I.D.; software, N.Č.; validation, N.Č. and I.D.; formal analysis, I.D.; investigation, N.Č. and I.D.; resources, I.D.; data curation, N.Č.; writing—original draft preparation, I.D.; writing—review and editing, N.Č. and I.D.; visualization, N.Č.; supervision, I.D.; project administration, N.Č.; funding acquisition, N.Č. All authors have read and agreed to the published version of the manuscript.

Funding: This research was funded by the University of Rijeka, Croatia, grant number uniri-iskusni-prirod-23-184 (Mathematical modeling of micropolar fluid and numerical spectral analysis using data-driven algorithms).

Data Availability Statement: The original contributions presented in this study are included in the article. Further inquiries can be directed to the corresponding author.

Conflicts of Interest: The authors declare no conflicts of interest.

References

1. Cosserat, E.; Cosserat, F. *Théorie des Corps déFormables*; Hermann et fils: Paris, France, 1909.
2. Eringen, A. Theory of thermomicrofluids. *J. Math. Anal. Appl.* **1972**, *38*, 480–496. [CrossRef]
3. Lukaszewicz, G. *Micropolar Fluids: Theory and Applications*; Birkhäuser: Basel, Switzerland, 1999.
4. Nowacki, W. *Theory of Micropolar Elasticity*; Springer: Berlin, Germany, 1974.
5. Papautsky, I.; Brazzle, J.; Ameel, T.; Frazier, A. Laminar fluid behavior in microchannels using micropolar fluid theory. *Sens. Actuators A Phys.* **1999**, *73*, 101–108. [CrossRef]
6. van der Waals, J. *Over de Continuïteit van den gas- en Vloeistoftoestand*; Numbers. 1 in Over de continuïteit van den gas- en vloeistoftoestand; Sijthoff: Amsterdam, The Netherlands, 1873.
7. Peng, D.; Robinson, D. A New Two-Constant Equation of State. *Ind. Eng. Chem. Fundam.* **1976**, *15*, 59–64. [CrossRef]
8. Batchelor, G.K. *An Introduction to Fluid Dynamics*, 2nd ed.; Cambridge University Press: Cambridge, UK, 1967.
9. Poling, B.E.; Prausnitz, J.M.; O'Connell, J.P. *The Properties of Gases and Liquids*, 5th ed.; McGraw-Hill: New York, NY, USA, 2001.
10. Gibson, J.F.; Halcrow, J.; Cvitanović, P. Equilibrium and travelling-wave solutions of plane Couette flow. *J. Fluid Mech.* **2009**, *638*, 243–266. [CrossRef]
11. Shelukhin, V.V. A shear flow problem for the compressible Navier-Stokes equations. *Int. J. Non-Linear Mech.* **1998**, *33*, 247–257. [CrossRef]
12. Shelukhin, V.V. A class of shear flows of a viscous compressible fluid. *J. Appl. Mech. Tech. Phys.* **1996**, *37*, 501–506. [CrossRef]
13. Qin, Y.; Rivera, J.E.M. Exponential stability and universal attractors for the Navier-Stokes equations of compressible fluids between two horizontal parallel plates in $\mathbb{R}^3$. *Appl. Numer. Math.* **2003**, *47*, 209–235. [CrossRef]
14. Zhou, W.; Qin, X.; Qu, C. Zero shear viscosity limit and boundary layer for the Navier-Stokes equations of compressible fluids between two horizontal parallel plates. *Nonlinearity* **2015**, *28*, 1721–1743. [CrossRef]
15. Cui, H.; Yao, Z.A. Asymptotic behavior of compressible p-th power Newtonian fluid with large initial data. *J. Differ. Equ.* **2015**, *258*, 919–953. [CrossRef]
16. Qin, Y.; Huang, L. Regularity and exponential stability of the pth Newtonian fluid in one space dimension. *Math. Models Methods Appl. Sci. M3AS* **2010**, *20*, 589–610. [CrossRef]
17. Wang, T. One dimensional p-th power Newtonian fluid with temperature-dependent thermal conductivity. *Commun. Pure Appl. Anal.* **2016**, *15*, 477–494. [CrossRef]
18. Wan, L.; Wang, T. Asymptotic behavior for the one-dimensional pth power Newtonian fluid in unbounded domains. *Math. Methods Appl. Sci.* **2015**, *39*, 1020–1025. [CrossRef]
19. Watson, S.; Lewicka, M. Temporal asymptotics for the p'th power Newtonian fluid in one space dimension. *Z. Angew. Math. Phys.* **2003**, *54*, 633–651. [CrossRef]
20. Yanagi, S. Asymptotic stability of the spherically symmetric solutions for a viscous polytropic gas in a field of external forces. *Transp. Theory Stat. Phys.* **2000**, *29*, 333–353. [CrossRef]
21. Lewicka, M.; Mucha, P. On temporal asymptotics for the pth power viscous reactive gas. *Nonlinear Anal. Theory Methods Appl.* **2004**, *57*, 951–969. [CrossRef]
22. Qin, Y.; Huang, L. Global Existence and Exponential Stability for the pth Power Viscous Reactive Gas. *Nonlinear Anal. Theory Methods Appl.* **2010**, *73*, 2800–2818. [CrossRef]
23. Qin, Y.; Huang, L. *Global Well-Posedness of Nonlinear Parabolic-Hyperbolic Coupled Systems*, 1st ed.; Frontiers in Mathematics; Birkhäuser: Basel, Switzerland, 2012. [CrossRef]

24. Béjar-López, A.; Cunha, C.; Soler, J. Two-dimensional incompressible micropolar fluid models with singular initial data. *Phys. D Nonlinear Phenom.* **2022**, *430*, 133069. [CrossRef]
25. Saad, E.; Faltas, M. Thermophoresis of a spherical particle straddling the interface of a semi-infinite micropolar fluid. *J. Mol. Liq.* **2020**, *312*, 113289. [CrossRef]
26. Yadav, P.; Verma, A. Analysis of immiscible Newtonian and non-Newtonian micropolar fluid flow through porous cylindrical pipe enclosing a cavity. *Eur. Phys. J. Plus* **2020**, *135*, 645. [CrossRef]
27. Nawaz, M.; Elmoasry, A.; Alebraheem, J.; Sajjad Saif, R. Impact of monocity and hybridity of nano-structures on thermal performance of micropolar fluid with novel heat flux theory: the Cattaneo—Christov heat flux theory. *J. Mater. Res. Technol.* **2020**, *9*, 8618–8626. [CrossRef]
28. Karvelas, E.G.; Tsiantis, A.; Papathanasiou, T.D. Effect of micropolar fluid properties on the hydraulic permeability of fibrous biomaterials. *Comput. Methods Programs Biomed.* **2020**, *185*, 105135. [CrossRef] [PubMed]
29. Baidya, U.; Das, S.; Das, S. Analysis of misaligned hydrodynamic porous journal bearings in the steady-state condition with micropolar lubricant. *Proc. Inst. Mech. Eng. Part J J. Eng. Tribol.* **2019**, *234*, 778–792. [CrossRef]
30. Mujakovic, N. One-dimensional flow of a compressible viscous micropolar fluid: A local existence theorem. *Glas. Mat. III. Ser.* **1998**, *33*, 71–91.
31. Dražić, I.; Mujaković, N. Local existence of the generalized solution for three-dimensional compressible viscous flow of micropolar fluid with cylindrical symmetry. *Bound. Value Probl.* **2019**, *2019*, 16. [CrossRef]
32. Bašić-Šiško, A.; Dražić, I. One-dimensional model and numerical solution to the viscous and heat-conducting reactive micropolar real gas flow and thermal explosion. *Iran. J. Sci. Technol. Trans. Mech. Eng.* **2022**, *47*, 19–39. [CrossRef]
33. Mujaković, N.; Črnjarić-Žic, N. Convergent finite difference scheme for 1D flow of compressible micropolar fluid. *Int. J. Numer. Anal. Model.* **2015**, *12*, 94–124.
34. Mujaković, N.; Črnjarić-Žic, N. Global solution to 1D model of a compressible viscous micropolar heat-conducting fluid with a free boundary. *Acta Math. Sci. Ser. B Engl. Ed.* **2016**, *36*, 1541–1576. [CrossRef]
35. Feireisl, E.; Novotný, A. Large time behaviour of flows of compressible, viscous, and heat conducting fluids. *Math. Methods Appl. Sci.* **2006**, *29*, 1237–1260. [CrossRef]
36. Smith, J.; Van Ness, H. *Introduction to Chemical Engineering Thermodynamics*, 7th ed.; McGraw-Hill: New York, NY, USA, 2001.
37. Maltese, D.; Michálek, M.; Mucha, P.B.; Novotný, A.; Pokorný, M.; Zatorska, E. Existence of weak solutions for compressible Navier—Stokes equations with entropy transport. *J. Differ. Equ.* **2016**, *261*, 4448–4485. [CrossRef]
38. Çengel, Y.A.; Boles, M.A. *Thermodynamics: An Engineering Approach*, 8th ed.; McGraw-Hill Education: New York, NY, USA, 2015.
39. Dražić, I.; Črnarić, N.; Simčić, L. A shear flow problem for compressible viscous micropolar fluid: Derivation of the model and numerical solution. *Math. Comput. Simul.* **2019**, *162*, 249–267. [CrossRef]
40. Antontsev, S.N.; Kazhikhov, A.V.; Monakhov, V.N. *Boundary Value Problems in Mechanics of Nonhomogeneous Fluids*; Studies in Mathematics and Its Applications; North-Holland Publishing Co.: Amsterdam, The Netherlands, 1990; Volume 22.
41. Ladyženskaja, O.; Solonnikov, V.; Ural'ceva, N. *Linear and Quasi-Linear Equations of Parabolic Type*; American Mathematical Society, Translations of Mathematical Monographs; American Mathematical Society: Providence, RI, USA, 1968.
42. Gottlieb, S.; Shu, C.W.; Tadmor, E. Strong stability-preserving high-order time discretization methods. *SIAM Rev.* **2001**, *43*, 89–112. [CrossRef]
43. Huang, L.; Bian, J.; Chen, Y. Large-time behavior of solutions to the compressible micropolar fluid with shear viscosity. *Discret. Contin. Dyn. Syst.-S* **2024**. [CrossRef]

Disclaimer/Publisher's Note: The statements, opinions and data contained in all publications are solely those of the individual author(s) and contributor(s) and not of MDPI and/or the editor(s). MDPI and/or the editor(s) disclaim responsibility for any injury to people or property resulting from any ideas, methods, instructions or products referred to in the content.